

Drag reduction by polymer additives in a turbulent pipe flow: numerical and laboratory experiments

By J. M. J. DEN TOONDER[†], M. A. HULSEN,
G. D. C. KUIKEN AND F. T. M. NIEUWSTADT

J.M. Burgers Centre, Laboratory for Aero- and Hydrodynamics,
Rotterdamseweg 145, 2628 AL Delft, The Netherlands

(Received 3 July 1995 and in revised form 28 November 1996)

In order to study the roles of stress anisotropy and of elasticity in the mechanism of drag reduction by polymer additives we investigate a turbulent pipe flow of a dilute polymer solution. The investigation is carried out by means of direct numerical simulation (DNS) and laser Doppler velocimetry (LDV). In our DNS two different models are used to describe the effects of polymers on the flow. The first is a constitutive equation based on Batchelor's theory of elongated particles suspended in a Newtonian solvent which models the viscous anisotropic effects caused by the polymer orientation. The second is an extension of the first model with an elastic component, and can be interpreted as an anisotropic Maxwell model. The LDV experiments have been carried out in a recirculating pipe flow facility in which we have used a solution of water and 20 w.p.p.m. Superfloc A110. Turbulence statistics up to the fourth moment, as well as power spectra of various velocity components, have been measured. The results of the drag-reduced flow are first compared with those of a standard turbulent pipe flow of water at the same friction velocity at a Reynolds number of $Re_\tau \approx 1035$. Next the results of the numerical simulation and of the measurements are compared in order to elucidate the role of polymers in the phenomenon of drag reduction. For the case of the viscous anisotropic polymer model, almost all turbulence statistics and power spectra calculated agree in a qualitative sense with the measurements. The addition of elastic effects, on the other hand, has an adverse effect on the drag reduction, i.e. the viscoelastic polymer model shows less drag reduction than the anisotropic model without elasticity. Moreover, for the case of the viscoelastic model not all turbulence statistics show the right behaviour. On the basis of these results, we propose that the viscous anisotropic stresses introduced by extended polymers play a key role in the mechanism of drag reduction by polymer additives.

1. Introduction

The addition of a minute amount of polymer to a turbulent Newtonian fluid flow can result in a large reduction of the frictional drag in pipes and channels. Although this effect has been known for almost half a century, the physical mechanism that causes this drag reduction has still not been clearly identified. Apart from the

[†] Present address: Philips Research, Prof. Holstlaan 4, 5656 AA Eindhoven, The Netherlands.

obvious practical applications, the phenomenon of drag reduction is also interesting from a fundamental point of view. Namely, the fact that small changes in fluid composition can so drastically alter the turbulent flow characteristics strongly hints that the polymer interferes with an essential mechanism of turbulent transport. That means that a study of polymeric drag reduction could help in gaining more insight into turbulence itself.

During the past three decades, a vast number of experimental papers have appeared on polymeric drag reduction, in particular in pipes and channels. Let us briefly review some of these experimental investigations. Among the recent studies are for example the contributions of Pinho & Whitelaw (1990), Harder & Tiederman (1991) and Wei & Willmarth (1992). These investigations have in common that they make use of laser Doppler velocimetry (LDV) to measure the turbulence statistics. Pinho & Whitelaw (1990) measure all three velocity components in a pipe flow, while the other two studies use a two-dimensional LDV system in a channel flow. Wei & Willmarth (1992) give special attention to the power spectra. One of the most striking results found in these papers, and also in the majority of other studies reported in the literature, is that polymer additives do not simply suppress the turbulent motion. On the contrary, the streamwise turbulence intensity is for example increased, while the normal turbulence intensity is decreased. This means that the turbulence structure is changed, rather than attenuated. Wei & Willmarth (1992) find that the energy in the normal velocity component is dramatically suppressed over all frequencies, while there is a redistribution of energy from high frequencies to low frequencies for the streamwise component. More experimental results reported in the literature will be discussed in §7. For an overview and more details the reader is referred to Tiederman (1990).

In spite of the large amount of observational data available, the mechanism of drag reduction by polymers still remains unclear. Therefore, another approach is called for. In our case, this is direct numerical simulation (DNS), which we use to obtain more insight into the mechanism of polymeric drag reduction in a rational way. Contrary to what is possible in experiments, one can try in numerical simulations to isolate certain properties of the polymer by using a specific constitutive equation, and to study in detail the effects that these properties have on the flow. In this way, the importance of these isolated properties for the phenomenon of drag reduction can be estimated, at least qualitatively.

The suitability of DNS for such a purpose has already been made clear in a previous paper (den Toonder, Nieuwstadt & Kuiken 1995*b*) where the role of extensional viscosity in the mechanism of drag reduction by polymer additives was investigated. The aim of that paper was to test a hypothesis introduced by Lumley (1969), who was the first to suggest that the molecular extension of polymers is responsible for drag reduction. Lumley argued that this extension will take place in the flow outside the viscous sublayer, causing an increase in effective viscosity there. Using general scaling arguments, Lumley showed that then a reduction in overall drag will occur. Den Toonder *et al.* (1995*b*) presented the results of a DNS with a simplified polymer extension criterion to increase the viscosity locally. It was found that a mere increase in effective viscosity outside the viscous sublayer is in itself not enough to produce significant drag reduction, so that Lumley's hypothesis should perhaps be made more specific. In particular we note that neither Lumley's hypothesis, although based on the notion of polymer extension, nor the rather simple model used in den Toonder *et al.* (1995*b*) contains any anisotropic stress effects caused by specific polymer orientations.

In the present paper, the numerical simulations started by den Toonder *et al.* (1995*b*)

are taken several steps further by incorporating anisotropic and elastic effects. That anisotropy might be important was suggested by the experiments performed by Virk & Wagger (1990). They studied the relation between the friction and the flow rate of polymer solutions in a turbulent pipe flow. The initial conformation of the polymers could be varied from extended to coiled by adding salt to the solvent. The result led to a higher drag reduction for the extended polymers, while at the same time the drag reduction onset Reynolds number[†] was found to be lower. This result suggests that the polymers are only effective when they take an elongated shape, like a rod or an extended thread, thereby introducing anisotropic effects in the fluid.

A theoretical study that supports the idea of anisotropy due to the extended polymers is given by Landahl (1973). He investigated the influence of different constitutive models on the stability of a conceptually simple turbulent flow model. The calculations performed with a Maxwell fluid model show destabilization of the flow for moderate amounts of elasticity. This is confirmed by the recent computations of Draad & Hulslen (1995). In the case of a Batchelor–Hinch model for rigid rods aligned in the mean-flow direction Landahl found a strong stabilizing effect. This led him to the conclusion that for polymeric drag reduction the anisotropic stress caused by the extension of the polymeric coils seems to be a key property, rather than viscoelasticity.

Recent experiments by Sasaki (1991*a, b*, 1992), who measured the effectiveness for drag reduction of various polymers in combination with several kinds of solvents, also suggest that the existence of rod-like entities in the solution which introduce anisotropic effects is essential. Moreover, he found that the drag-reducing ability of polymer solutions tends to decrease when the polymers become more flexible, which is also in accordance with Landahl (1973). Finally, we should mention that the possibility of drag reduction as being an anisotropic response of the flow to an anisotropic viscosity induced by elongated polymers has been also suggested by Hinch (1977).

On the other hand, de Gennes (1990) and Joseph (1990) suggest quite another mechanism to explain drag reduction by polymers. They maintain that it is elasticity which is responsible. A polymer solution, even a very dilute one, can be regarded as a viscoelastic fluid. In these fluids the viscosity takes care of diffusion and of the smoothing of shear discontinuities ('shear waves'), while on the other hand the elasticity is able to propagate these shear discontinuities. Moreover, in purely viscous fluids, the stress is always in phase with the rate of strain in the flow while in viscoelastic fluids, this is generally not the case. This is related to the fact that polymers are in principle capable of storing elastic energy. In the view of Joseph (1990), the characteristic speed of shear waves in polymer solutions (see Joseph *et al.* 1986) provides a natural cut-off for velocities which fluctuate at high frequencies. In fact the fluctuating velocities which are observed in turbulent flow of aqueous drag-reducing solutions are of the right order, namely a few centimetres per second, for such a cut-off to be important. This cut-off would then suppress the small eddies and presumably lead to drag reduction.

De Gennes (1990) also states that the effects of polymers at high frequencies are described by an elastic modulus, resulting in a truncation of the turbulent velocity fluctuations at these frequencies. Using a simple scaling analysis and an elastic model

[†] From experiments it is found that drag reduction only occurs if a certain wall shear stress, or Reynolds number is exceeded. This drag reduction onset Reynolds number is dependent on the type of fluid used (see e.g. Virk 1975).

for the polymer solution, he indeed finds that drag reduction might occur through such a mechanism. His analysis however suffers from the shortcomings that it is rather crude and it is not able to explain the detailed dynamics of wall turbulence.

The purpose of the present paper is to shed more light on the role of anisotropy and elasticity in polymeric drag reduction. To that end, we have performed a DNS of a turbulent pipe flow for a viscous anisotropic and for a viscoelastic anisotropic fluid. For the first fluid, we have used a constitutive model based on Batchelor's theory of suspensions of elongated particles. Although this constitutive model is a rather crude representation of a dilute solution of elongated polymers, we nevertheless believe that it is able to capture the essence of the viscous anisotropic stresses connected to stretched polymer molecules. Hence, the results of our simulation will reflect the influence of this isolated effect of the polymers on the turbulence. The second fluid model is an anisotropic Maxwell model, and consists of an extension of the first model with an elastic component. Comparison of the results obtained with both models may give us an indication of the role of elasticity in polymeric drag reduction. In combination with the numerical simulations, we have conducted measurements in a turbulent pipe flow with water and with a dilute polymer solution. The observations have been carried out with the aid of a two-component LDV system. We have been able to obtain information on the turbulence statistics up to fourth order in the near-wall region. We have also measured turbulent power spectra at several radial positions in the pipe.

The plan of the remainder of this article is as follows. After the formulation of the basic equations in §2, we formulate the viscous anisotropic polymer model in §3, and the viscoelastic anisotropic model in §4. In §5 the numerical procedures of the calculations are briefly described. Section 6 contains a description of the experiment, including the flow loop, the LDV setup, the polymer solution and the experimental conditions. In §7 the results of both the numerical simulations and the LDV measurements are presented. Finally, §8 contains the conclusions drawn from the results and a discussion is presented focusing on a possible mechanism for polymeric drag reduction.

2. Basic equations

We consider a fluid that consists of a Newtonian solvent to which a minute amount of polymer is added. The basic equations that describe the incompressible flow of such a fluid are given by

$$\nabla \cdot \mathbf{u} = 0, \quad (2.1)$$

$$\rho \frac{D\mathbf{u}}{Dt} = -\nabla p + \nabla \cdot \boldsymbol{\tau}. \quad (2.2)$$

In these equations \mathbf{u} is the velocity vector, ρ is the density, p is the pressure and $\boldsymbol{\tau}$ is the deviatoric stress tensor. D/Dt denotes the material derivative. The first equation is the continuity equation and the second the linear-momentum equation.

To close the problem, a relation must be given that expresses the stress $\boldsymbol{\tau}$ in terms of the deformation history. To this end we split the stress tensor $\boldsymbol{\tau}$ into two parts, namely a part due to the Newtonian solvent and a non-Newtonian part caused by the polymers:

$$\boldsymbol{\tau} = \boldsymbol{\tau}_N + \boldsymbol{\tau}_P. \quad (2.3)$$

For τ_N the well-known Newtonian constitutive equation is valid:

$$\tau_N = 2\mu\mathbf{D}, \quad (2.4)$$

where μ is the dynamic viscosity, $\mathbf{D} = (\mathbf{L} + \mathbf{L}^T)/2$ is the rate-of-strain tensor in which $\mathbf{L} = (\nabla\mathbf{u})^T$ is the velocity gradient tensor. For the non-Newtonian stress τ_p however, a different equation must be supplied, which will depend on the special properties of the polymers. This is considered in the following sections for a viscous anisotropic fluid and for a viscoelastic anisotropic fluid.

3. Viscous anisotropic (VA) model

To study the role played by the anisotropy due to extended polymers in the process of drag reduction, we use a constitutive model derived by Batchelor (1971) for a suspension of elongated particles. The rationale for using this model is that polymers that are supposedly stretched out greatly in a certain direction act hydrodynamically as elongated particles.

The model given by Batchelor (1971) in the limit of high aspect ratio and no Brownian motion is

$$\tau = \tau_N + \tau_p = 2\mu\mathbf{D} + \mu_2\mathbf{D} : \mathbf{n}\mathbf{n}\mathbf{n}\mathbf{n}, \quad (3.1)$$

where the unit vector, \mathbf{n} , gives the orientation of the particles. It follows from:

$$\frac{D\mathbf{n}}{Dt} - \boldsymbol{\Omega} \cdot \mathbf{n} = \mathbf{D} \cdot \mathbf{n} - (\mathbf{n} \cdot \mathbf{D} \cdot \mathbf{n})\mathbf{n}. \quad (3.2)$$

The μ_2 in (3.1) is a constant that can be related to the solvent viscosity μ and the particle properties by

$$\mu_2 = \frac{\pi\mu N_p l^3}{6 \ln(l/a)}, \quad (3.3)$$

where N_p is the number density of particles, l their length and a their radius.

Strictly speaking this constitutive equation is valid only if the suspension is dilute in the sense of negligible particle interactions, i.e. it is required that $(\mu_2/\mu) \ll 1$ (see Batchelor 1971). However, Batchelor (1971) also showed that the form of equation (3.1) is retained for larger concentrations, but with a different expression for μ_2 , namely

$$\mu_2 = \frac{\pi\mu N_p l^3}{6 \ln(h/a)}, \quad (3.4)$$

where $h = (N_p l)^{-1/2}$ is the average interparticle spacing for a locally aligned distribution of particles. This expression is applicable when both $l \gg h \gg a$ and the particle concentration is not so small that the suspension is dilute in the sense of negligible particle interactions, see Batchelor (1971).

Let us make an estimation of the value of μ_2/μ for our drag-reducing polymer solution according to the expressions above under the assumption that the polymers are fully elongated. For linear, high-molecular-weight polymers (with a molecular weight of the order 10^6 g mol⁻¹), the following typical values apply: the total length of a molecule equals $l \approx 30$ μm , and its thickness is $a \approx 0.3$ nm. For a concentration of 20 w.p.p.m., $N_p \approx 3 \times 10^{18}$ m⁻³. Therefore, $\mu_2/\mu \approx 4000$ if (3.3) is used, which falls outside the applicability range of this equation. On the other hand, $h \approx 0.1$ μm , so that (3.4) may be applied and this equation gives $\mu_2/\mu \approx 7000$.

Applying the model given by (3.1) and (3.2) in combination with the basic equations

(2.2) and (2.3) to a DNS of a turbulent flow leads to very large problems in terms of computing capacity and computing time. What is worse is that the lack of any diffusion of \mathbf{n} could lead to computationally impossibly high spatial gradients of \mathbf{n} , in particular at boundaries (see e.g. Lipscomb *et al.* 1988).

Therefore, we have turned to an alternative way of solving (approximately) the problem with an acceptable computational effort. There are a number of *ad-hoc* ways of dealing with the aforementioned problems. The most reasonable one is to employ the so-called ‘aligned particle approximation’, which is based on the observation that large-aspect-ratio fibres often align quickly with the flow direction (e.g. Stover, Koch & Cohen 1992; Papanastasiou & Alexandrou 1987). In fact, it can be shown that the orientation parallel to the velocity is always a steady solution of (3.2) (see Keiller & Hinch 1991). In that case

$$\mathbf{n} = \frac{\mathbf{u}}{|\mathbf{u}|}. \quad (3.5)$$

The application of approximation (3.5) to an inherently unsteady flow, such as our turbulent pipe flow, is questionable since this solution of (3.2) is strictly only valid for steady flows. It is however the best alternative within our computational limitations. The approximation may be not so bad if one considers that turbulent flow through a straight pipe can be viewed as a shear flow with in addition small perturbations due to the turbulent fluctuations. Therefore, for the turbulent pipe flow, the average direction of the particles can be expected to point in the flow direction.

By applying the aligned-particle approximation, our anisotropic model for the stress becomes

$$\boldsymbol{\tau} = \boldsymbol{\tau}_N + \boldsymbol{\tau}_P = 2\mu\mathbf{D} + \mu_2\mathbf{D} : \frac{\mathbf{u}\mathbf{u}\mathbf{u}\mathbf{u}}{(\mathbf{u} \cdot \mathbf{u})^2}. \quad (3.6)$$

We call this the viscous anisotropic model (VA model), because it describes a purely viscous effect, as will be explained in the next section.

The shear viscosity of a dilute polymer solution is not much different from the Newtonian shear viscosity of the solvent. Measurements by Draad (1996) of a 20 w.p.p.m. solution of polyacrylamide in tap water using a low-shear viscosimeter show a slight increase of the zero-rate viscosity and shear-thinning behaviour of non-degraded polymers. Since we want to separate the anisotropic behaviour of the fluid from other effects, we neglect this slight change in the shear viscosity. Indeed, equation (3.6) predicts in pure shear a constant shear viscosity μ , equal to that of the solvent. In extensional flow, on the other hand, the uniaxial extensional viscosity of model (3.6) is

$$\eta_E = 3\mu + \mu_2, \quad (3.7)$$

whereas the biaxial extensional viscosity is

$$\eta_B = 6\mu + \frac{1}{2}\mu_2. \quad (3.8)$$

Hence, by setting the parameter μ_2 we can increase the extensional viscosities above their Newtonian value. This agrees at least qualitatively with the behaviour found in dilute polymer solutions for η_E as observed by for example Metzner & Metzner (1970), James & Saringer (1980), and Fruman & Barigah (1982). These authors found that η_E could be increased by even several orders of magnitude for dilute polymer solutions; this is consistent with our estimation of $\mu_2 \approx 7000\mu$, given above. However, practical computational restrictions impose a limit on the value of μ_2 , as will be explained in §5. Therefore, we have limited the computations to two rather low values of μ_2 , namely $\mu_2 = 12\mu$ and 27μ respectively. This means that according to (3.7) the

uniaxial extensional viscosity of the anisotropic fluid equals $\eta_E = 15\mu$ respectively 30μ . For Newtonian fluids, $\eta_E = 3\mu$ and hence, η_E is increased by a factor of 5 respectively 10 with respect to the Newtonian value. Similarly, it follows from (3.8) for the biaxial extensional viscosity that $\eta_B = 12\mu$ respectively 19.5μ , which is twice respectively 3.25 times the Newtonian value. Note that the change in extensional viscosity is different for the uniaxial and the biaxial cases. Because of these rather low values, we may expect no quantitative agreement for our DNS results with the results of the measurements of drag-reduced flows. However, the DNS results can be compared with the measurements in a qualitative sense and as we will see later, the tendencies that we find with our model seem to follow the measurements correctly.

It may further be noted that the first and second normal stress differences, N_1 and N_2 , are both equal to zero for model (3.6). The quantities N_1 , N_2 and η_B have, to our knowledge, not been measured for dilute polymer solutions such as we have used in this study (20 w.p.p.m.). Hence, it cannot be claimed with certainty that the present model has the correct behaviour for these parameters.

It will be clear that the model (3.6) is a rather simplistic representation of a dilute solution of elongated polymers. Computational limitations have demanded this simplicity, and have also been the cause of the need to restrict μ_2 to rather low values. Nevertheless, our model seems to be a reasonable first approximation for modelling the anisotropic stresses related to stretched polymer molecules if one assumes that their hydrodynamic effect is similar to that of elongated particles, as has been suggested by Batchelor (1971), Bark & Tinoco (1978), Keiller & Hinch (1991), and others. As such, we believe that using (3.6) in a turbulent pipe flow simulation will give us insight into the role played in the process of drag reduction by elongated polymers.

4. Viscoelastic anisotropic (VEA) model

The VA model (3.6) describes a purely viscous process, i.e. the stress is always in phase with the rate of strain and no elastic effect is involved. This can be represented by a mechanical model. Mechanical models provide a popular method of visualizing linear viscoelastic behaviour in general. These one-dimensional models consist of a set of springs and dash-pots so arranged that the overall system has a response like a real material, although the elements themselves may have no direct analogues in the actual material. The correspondence between the behaviour of the model and the real material is achieved if the differential equation relating the force, extension and time for the model is the same as the equation relating stress, strain and time for the material.

The mechanical counterpart representing the non-Newtonian part of the VA model (3.6) is depicted in figure 1(a). It consists of a dash-pot with viscosity μ_2 acting only in the direction of \mathbf{u} . In this direction, the equation relating the strain (extension) ϵ to the stress (force) σ is

$$\sigma = \mu_2 \dot{\epsilon}. \quad (4.1)$$

Translating this picture to the three-dimensional situation, and remembering that the damping action of the dash-pot is restricted to the \mathbf{u} -direction only, we obtain

$$\boldsymbol{\tau}_P = \mu_2 (\mathbf{u} \cdot \mathbf{D} \cdot \mathbf{u}) \mathbf{u} \mathbf{u} / |\mathbf{u}|^4. \quad (4.2)$$

Here $\mathbf{u} \cdot \mathbf{D} \cdot \mathbf{u} / |\mathbf{u}|^2$ is the projection of the three-dimensional rate of strain on the direction of $\mathbf{u} / |\mathbf{u}|$, and the vector product $\mathbf{u} \mathbf{u} / |\mathbf{u}|^2$ appears because the stress tensor

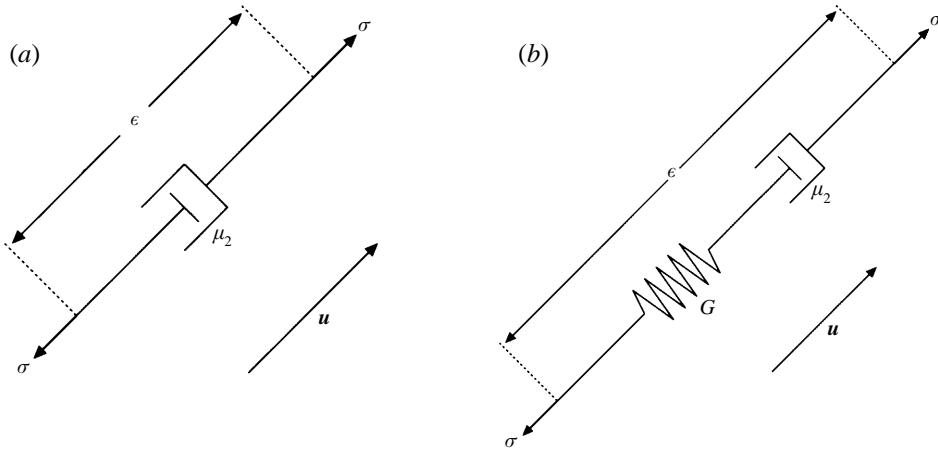


FIGURE 1. Mechanical model of (a) the viscous anisotropic model, and (b) the viscoelastic anisotropic model.

τ_P must have a component in the direction of \mathbf{u} only. Equation (4.2) is precisely the non-Newtonian part of the VA model (3.6).

This purely viscous mechanical model can now be extended with an elastic component. A possible way to do this is shown in figure 1(b), in which a spring with elastic modulus G is added in series to the dash-pot. Both components of the model act only in the direction of \mathbf{u} . The equation relating the strain (extension) ϵ to the stress (force) σ in case of figure 1(b) now becomes

$$\lambda \dot{\sigma} + \sigma = \mu_2 \dot{\epsilon}, \quad (4.3)$$

in which $\lambda = \mu_2/G$ is the characteristic relaxation time of the system. The three-dimensional analogue of (4.3) can now be written as

$$\left. \begin{aligned} \tau_P &= F \mathbf{u} \mathbf{u} / (\mathbf{u} \cdot \mathbf{u}), \\ \lambda \dot{F} + F &= \mu_2 (\mathbf{u} \cdot \mathbf{D} \cdot \mathbf{u}) / (\mathbf{u} \cdot \mathbf{u}). \end{aligned} \right\} \quad (4.4)$$

This model can be interpreted as an anisotropic variant of the classical linear Maxwell fluid model. If viscous effects dominate over elastic effects, then (4.4) reduces to (4.2), but if elastic effects dominate, (4.4) represents a Hookean-type material.

Summarizing, our viscoelastic anisotropic model (VEA model) now reads

$$\boldsymbol{\tau} = 2\mu \mathbf{D} + \boldsymbol{\tau}_P, \quad (4.5)$$

in which $\boldsymbol{\tau}_P$ is given by (4.4).

We stress that we do not pretend that this model gives an adequate representation of the elastic properties of a dilute polymer solution. It is merely the simplest extension of the anisotropic fluid model (3.6) with an elastic effect. Because of the anisotropy of the model, the elasticity will be present only in flow deformations with an extensional component, so that, strictly speaking, the model is incapable of propagating shear waves. Nevertheless, we believe that our simulation in which we have used the viscoelastic anisotropic model is able to give some indication of the importance of elastic effects for polymeric drag reduction.

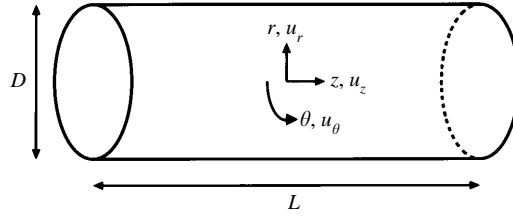


FIGURE 2. Computational domain and notation convention of the direct numerical simulation.

5. Numerical procedure

For the DNS of a turbulent pipe flow with the fluids defined by the models proposed in §§3 and 4, we used a numerical code formulated in a cylindrical geometry. A full account of the numerical procedures can be found in Eggels (1994), Pourquié (1994), or Eggels *et al.* (1994). In this section only the essentials are summarized.

The cylindrical pipe geometry is shown in figure 2. The diameter of the pipe is denoted by D and the pipe length by L with $L = 5D$. In this geometry, (2.1) and (2.2) were solved, using the VA and the VEA model, respectively. The equations were made dimensionless with the friction velocity u_τ , the pipe diameter D and the fluid density ρ . The friction velocity is defined as $\rho u_\tau^2 = \tau_w$, in which τ_w is the mean shear stress at the wall. The equations then read

$$\nabla^* \cdot \mathbf{u}^* = 0, \quad (5.1)$$

$$\frac{D\mathbf{u}^*}{Dt^*} = -\nabla^* p^* + \nabla^* \cdot \boldsymbol{\tau}^*, \quad (5.2)$$

in which the asterisk denotes a non-dimensional quantity. The expression for $\boldsymbol{\tau}^*$ depends on the model used. For the VA model the following equation applies (see (3.6)):

$$\boldsymbol{\tau}^* = \frac{2}{Re_\tau} \mathbf{D}^* + \mu_2^* \mathbf{D}^* : \frac{\mathbf{u}^* \mathbf{u}^* \mathbf{u}^* \mathbf{u}^*}{(\mathbf{u}^* \cdot \mathbf{u}^*)^2}. \quad (5.3)$$

The Reynolds number Re_τ is defined as $Re_\tau = u_\tau D / \nu$, where $\nu = \mu / \rho$ is the Newtonian kinematic viscosity. The equation for the VEA model (see (4.4)) reads

$$\boldsymbol{\tau}^* = \frac{2}{Re_\tau} \mathbf{D}^* + F^* \frac{\mathbf{u}^* \mathbf{u}^*}{\mathbf{u}^* \cdot \mathbf{u}^*}, \quad (5.4)$$

$$\lambda^* \frac{D F^*}{Dt^*} + F^* = \mu_2^* \frac{\mathbf{u}^* \cdot \mathbf{D}^* \cdot \mathbf{u}^*}{\mathbf{u}^* \cdot \mathbf{u}^*}. \quad (5.5)$$

In all calculations, the Reynolds number Re_τ was set at 360. This corresponds to $Re = U_b D / \nu = 5300$ in a turbulent pipe flow of a Newtonian fluid where U_b is the bulk mean velocity. Fixing Re_τ at a certain value is equivalent to keeping the pressure gradient constant. Therefore, a possible drag reduction would manifest itself as an increase of the flow rate in our computations.

We performed two simulations with the VA model, the first with $\mu_2^* = 12/Re_\tau = 0.033$, and the second with $\mu_2^* = 27/Re_\tau = 0.075$. In the simulation with the VEA model, (5.4)–(5.5), we put $\mu_2^* = 12/Re_\tau$, i.e. equal to the value used in the first simulation with the VA model. The non-dimensional relaxation time was taken to be $\lambda^* = 0.02$. It will be shown in §7 that with this choice the VEA model simulation has

resulted in viscous and elastic contributions to the stress in equation (5.5) which are of the same order of magnitude.

Equations (5.1)–(5.5) were discretized with a second-order finite volume technique on a staggered grid. For the time integration, the advection terms in (5.2) and (5.5) containing derivatives in the circumferential direction, the source term in (5.5) and the Newtonian diffusion terms containing derivatives in the circumferential direction were treated implicitly. For the advection terms the Crank–Nicholson scheme was used and for the source term and for the diffusion terms the Euler-backward scheme. All other terms were advanced in time using an explicit scheme, namely the lagged Euler-forward scheme for the remaining Newtonian diffusion terms and the leapfrog method for the remaining advection terms and also for all non-Newtonian stress terms in the VA and VEA models.

The computations were carried out with $96 \times 128 \times 256$ grid points equally spaced in r -, θ -, z -directions respectively. As discussed in Eggels *et al.* (1994), this resolution is sufficient to resolve all turbulent length scales. The time step Δt was computed interactively using a criterion to avoid numerical instabilities (Schumann 1975; Pourquié 1994). The mean value of Δt^* was approximately 0.00011 for the first VA and the VEA simulation, and 0.000036 for the second VA simulation. These values were well below the smallest turbulent time scale in the pipe flow. The small value of Δt was due to time-explicit treatment of the non-circumferential and the non-Newtonian terms. Through these terms Δt is directly coupled to the value of μ_2 in the anisotropic models: the larger μ_2 , the smaller Δt must be chosen for the numerics to remain stable. This imposes a practical limit for the value of μ_2 , to which we have already referred above.

The simulations, with the exception of the second VA simulation, were initiated from a fully developed turbulent field of a Newtonian fluid at $Re_\tau = 360$ obtained by Eggels *et al.* (1994). At $t^* = 0$ the polymer model was turned on. After a development period of $10t^*$, which is $10D/u_\tau$, the computations were continued for an additional $4t^*$ during which data fields were stored every $0.1t^*$. In post-processing algorithms, these data fields have been used to compute the various statistical results to be presented in §7. The time separation of $0.1t^*$ between two sequential data fields was large enough compared to the integral time scale of the turbulent fluctuations for the data fields to be nearly independent realizations of the flow. The flow statistics have been obtained by spatial averaging in the homogeneous streamwise (z) and circumferential (θ) directions and by temporal (or ensemble) averaging over all stored data fields. Statistics obtained in such a way are denoted by an overbar in the following sections.

The second VA simulation was initiated from the final data field of the first VA simulation at $t^* = 14$ and continued until $t^* = 25$. The turbulence statistics have in this case been computed from data fields collected between $t^* = 20.2$ and $t^* = 24.5$ using the same procedure as described in the previous paragraph.

The simulations were carried out on the Cray Y-MP C98/4256 computer of the Academic Computing Services Centre (SARA) in Amsterdam. The computational requirements were as follows. For the first VA-model simulation, a memory of 92.3 Mwords (=738 Mbyte) was required, the execution of one time step took 5.4 s, and about 190 h was needed to perform the full simulation. For the second VA simulation, these values were 92.3 Mwords, 5.3 s and 450 h, respectively. Finally, the VEA simulation required 98.5 Mwords (=788 Mbyte) of memory, the CPU-time to perform one timestep was approximately 5.7 s, and about 200 h was needed to carry out the total simulation. These values underline the limitation that we had to put on the value of μ_2 .

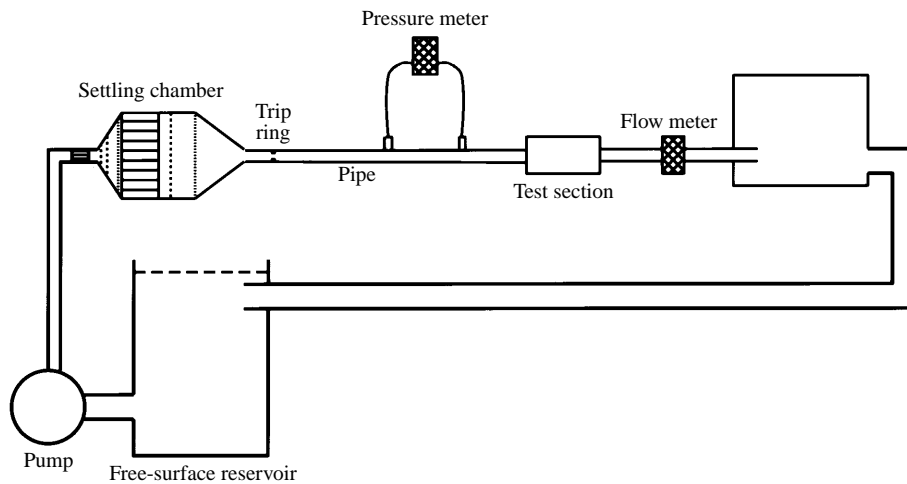


FIGURE 3. The pipe flow facility.

6. Description of the experimental set-up

In this section we briefly describe the experimental set-up. A more detailed treatment can be found in den Toonder (1995) and Draad (1996).

6.1. The pipe flow loop

The laboratory experiments were performed in the re-circulatory pipe flow facility of the Laboratory for Aero- and Hydrodynamics. A schematic diagram of this facility is shown in figure 3. An extensive description of this set-up and its various design details can be found in Draad (1996). The total volume of the system is 1.4 m³. The main part of the facility consists of a cylindrical Perspex pipe with length 34 m and inner diameter 40 mm. The pump used is a so-called disk pump, manufactured by Begemann. This type of pump avoids strong degradation of the polymers (den Toonder *et al.* 1995a). Before entering the pipe, the fluid passes first through a flow straightening device and then through the settling chamber, which contains another flow straightening device as well as several screens. The transition to the pipe consists of a smooth contraction. At a distance of 1 m behind the settling chamber a so-called 'trip ring' is inserted in the pipe to force transition to turbulence. To avoid secondary circulation due to free convection, the entire pipe is insulated with 3 cm Climaflex pipe insulation. In the whole set-up no contact of the fluid with metals is allowed, because the polymers are damaged by metal ions, i.e. zinc, copper or iron.

The pressure gradient along the pipe is measured with a membrane differential-pressure transducer (Validyne Engineering Corp., type DP15-20) between the positions 18 m and 28 m behind the settling chamber. The flow rate is observed with a magnetic inductive flow meter (Krohne Altometer, type SC 100 AS). The temperature of the fluid is measured with a thermocouple in the free-surface reservoir. The measurement data of the pressure gradient, flow rate and temperature are sampled automatically with a PC.

The curvature of the pipe wall leads to problems in measuring very close to the wall with LDV because of the refraction of the laser beams by the curved pipe wall. This difficulty arises because of the differences in refractive index of the test fluid (i.e. water with $n = 1.33$) and the material of the pipe (i.e. Perspex with $n = 1.49$). To minimize this problem, we have designed a special test section, illustrated in figure 4.

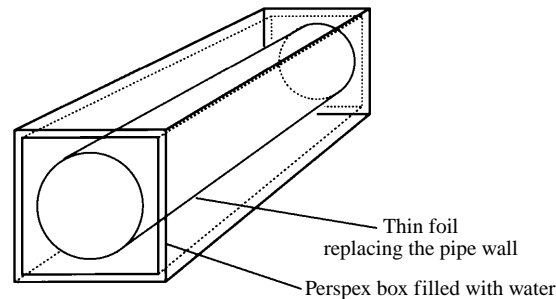


FIGURE 4. The test section.

In the test section, located 30 m downstream of the inlet of the pipe, the pipe wall is partly replaced by a thin foil made of Teflon FEP (fluorized ethylene propylene) with a thickness of $190\ \mu\text{m}$, kindly provided by Du Pont de Nemours. This material has a refractive index of $n = 1.344 \pm 0.003$, which is quite close to that of our test fluid. The use of this foil in combination with the square Perspex box filled with water around the cylindrical foil minimizes the refraction errors of the laser beams. As a result we can perform measurements down to a distance of 0.2 mm from the wall, which is about 5 viscous lengths for the measurements presented in this paper. The inner diameter of the pipe segment formed by the foil is 40.37 mm. The walls of the Perspex box have a thickness of 6 mm while the distance of these walls to the pipe centre is 60 mm.

6.2. *The LDV set-up*

The measurements were performed with a 2-component LDV system manufactured by Dantec. This system uses two orthogonal pairs of laser beams with pairwise light of a different wavelength to measure the fluid velocity in two directions. Each of the pairs forms a so-called ‘measurement volume’ at the position where the two beams intersect. The light that is scattered by a particle travelling through the measurement volume is collected in the backscattered direction. The optics to focus the laser beams into the pipe and also to receive the scattered light is built in one measuring probe (Dantec) with a focusing front lens with focal length 80 mm. This probe is attached to a three-dimensional traversing system also supplied by Dantec. The probe is connected to an Argon-ion laser of Spectra Physics (model 2020) via a fibre and a transmittorbox. The transmittorbox splits up the light coming from the laser into two wavelengths, namely 514.5 nm and 488 nm (one for each laser beam pair), and feeds it into the fibre through which the light travels to the measuring probe. At the same time, the fibre carries the backscattered laser light from the probe back to two photo-multiplier (PM) tubes, via the transmittorbox and a colour separator that separates the two colours. The output from the PM tubes goes to two “Burst Spectrum Analyzers” (Dantec, type Enhanced 57N20 and Enhanced slave 57N35), one for each laser beam pair, or velocity component. By means of a spectral analysis of the signal, each BSA computes the Doppler shift between the transmitted and the scattered light, and this shift is proportional to the velocity component of the particle perpendicular to both beams.

The streamwise (or axial) velocity component was measured using the 488 nm laser beam pair, and the normal (or radial) component with the 514.5 nm pair. The dimensions of the measurement volumes are estimated to be 20, 20 and 100 μm in the streamwise, normal and spanwise directions respectively.

In all measurements to be presented later in this paper, the probe was traversed in the vertical direction. As a result the measurement volumes travelled along a vertical plane through the central axis of the pipe, so that at each position we measured the axial and radial velocity components.

In all experiments the fluid was seeded with pigment based on TiO_2 to get high data rates. The power supplied by the laser was always 2.5 W, corresponding to a power of approximately 150 mW in each laser beam.

6.3. The polymer solution

The polymer that we used in our experiments is Superfloc A110 (Cytec Industries), which is a partially hydrolysed polyacrylamide (PAMH). Superfloc A110 has a molecular weight of $6\text{--}8 \times 10^6 \text{ g mol}^{-1}$, according to the manufacturer. The advantage of this polymer over other types of polymer encountered in the literature (e.g. Polyox WSR301, Union Carbide, or Separan AP273, Dow Chemical Company), is that it is relatively resistant to mechanical degradation (see den Toonder *et al.* 1995a). Mechanical degradation is the breaking of the polymers by mechanical action, which reduces their molecular weight and thus their capability for drag-reduction (see Virk 1975). This is an important point, since we use a re-circulatory experimental set-up in which the polymers are continuously subjected to deformations, especially in the pump, which might cause the scission of the polymers. Severe mechanical degradation leads to unacceptable changes in the measurement conditions during an LDV measurement. The use of Superfloc A110 in combination with the disk pump minimizes this problem, as shown in den Toonder *et al.* (1995a). Nevertheless, there was always some degradation present, particularly when a solution was fresh. To ensure during our LDV measurements virtually stationary drag reduction, the set-up was operated for about 20 hours after the addition of the polymer, before the actual LDV measurements were started. During this period, the drag reduction decreased from approximately 70% to about 20%, due to degradation. After this intentional degradation, LDV measurements under constant polymer conditions were possible.

In the experiments presented in this paper we used a Superfloc A110–water solution with a polymer concentration of $C_p = 20 \text{ w.p.p.m.}$ That means that only 28 g of polymer was dissolved in the entire system. First a 1000 w.p.p.m. master solution was prepared in a self-made stirring vessel as follows. The vessel was filled with 70 l of “Delft” tap water. A total amount of 70 g of Superfloc A110 was divided into seven equal portions. Each of the portions was dissolved in 0.3 l ethanol. The seven suspensions thus obtained were then added to the tap water in the vessel while stirring which created a large vortex in the vessel. For the next two hours the solution was mixed gently. After this period, the solution contained small air bubbles, that were allowed to escape in the following 24 hours. At the end of this procedure, the solution obtained was visibly clear and it did not contain any detectable inhomogeneities.

The 1000 w.p.p.m. solutions prepared in this way were used in the pipe set-up within 1 to 2 weeks. To obtain the desired concentration, i.e. 20 w.p.p.m., 28 l of the 1000 w.p.p.m. solution were added in the free-surface reservoir (see figure 3) and mixed by hand, while at the same time the pump operated to obtain a flow rate of approximately 3000 l h^{-1} to mix the polymer in the entire set-up.

6.4. The experimental conditions

We conducted measurements of the turbulent pipe flow of tap water and polymer solutions in the range $Re_\tau \approx 340$ to ≈ 1400 . In this paper we will only give the results for $Re_\tau \approx 1035$, larger than the Re_τ at which the computations were performed,

Symbol used in figures	Profile measurements		Spectrum measurements	
	■	□	◆	◇
C_p (w.p.p.m.)	0	20	0	20
u_τ (mm s ⁻¹)	27.8	27.7	27.7	27.6
ν/u_τ (mm)	0.0388	0.0391	0.0390	0.0395
Q (h ⁻¹)	2191	2870	2180	2469
$Re = U_b D/\nu$	17773	23281	17680	19844
$Re_\tau = u_\tau D/\nu$	1039.2	1033.5	1035.4	1022.2
DR (%)	-	24.2	-	12.2

TABLE 1. Experimental conditions of the measurements.

i.e. 360. The reason is, that at the lowest Reynolds number in the measurements the observed drag reduction was negligible after the intentional degradation period mentioned in the previous section because the wall shear stress turned out to be too small for drag reduction to occur in that case. Hence, it was impossible to carry out LDV measurements under stationary polymer conditions for $Re_\tau \approx 340$. The complete set of the measured data can be found in den Toonder (1995). It may be noted here that the results for the measurement with pure water at $Re_\tau \approx 340$ agree with the data presented in Eggels *et al.* (1994) for $Re_\tau = 360$.

Table 1 lists the experimental conditions of the measurements. In the first row the symbols are shown which will be used in the figures in the remainder of this paper for the corresponding measurements. We performed two types of measurement, which were carried out independently, namely profile measurements from which profiles of turbulence statistics have been computed, and spectrum measurements from which turbulent power spectra have been determined.

The mean data rate in the profile measurements was $f_{dr} \approx 60$ Hz, and the measurement time per position was $T = 300$ s. The spectrum measurements were performed at three different positions in the pipe: $y^+ \approx 12, 30$ and 125 . The mean sampling rate at these positions was approximately 2400, 3000 and 4000 Hz respectively. In the spectrum measurements, each time series consisted of approximately 196 000 samples.

A concentration $C_p = 0$ denotes a measurement with pure water (i.e. ‘‘Delft’’ tap water).

The measurements for water and polymer solution are compared at (almost) equal friction velocity u_τ . This quantity has been determined from the pressure measurements according to

$$u_\tau = \left(\frac{D}{4\rho} \left| \frac{\Delta P}{\Delta z} \right| \right)^{1/2}, \quad (6.1)$$

where D is the diameter of the pipe, ΔP the measured pressure difference and Δz the distance over which ΔP is measured.

The viscous length scale ν/u_τ is composed of the kinematic viscosity of the fluid, ν , and the friction velocity. For ν , the value which applies to water has been used in the polymer solution measurements as well, based on the assumption that the small polymer concentration used does not alter the shear viscosity of the fluid. The value of ν has been calculated at the temperature measured in the pipe.

The Reynolds number Re is defined with the bulk velocity in the pipe, i.e. $Re = U_b D/\nu$, and has been determined from the measured flow rate Q . The Reynolds

number Re_τ is defined with the friction velocity: $Re_\tau = u_\tau D/\nu$. The centre of the pipe in wall units thus is given by $Re_\tau/2$.

The amount of drag reduction has been computed from the measured flow rate with the equation

$$DR = \left(1 - \frac{Q_N}{Q_P}\right) \times 100\%, \quad (6.2)$$

in which the subscript N denotes the Newtonian fluid, and the subscript P the polymer solution. The values of DR in our experiments are rather lower than previously reported values because of the intentional degradation of the polymers before measuring with LDV, as described in §6.3. Still, the influence of the polymers is quite clear, as will be shown in §7.

6.5. Processing of the LDV data

The turbulence statistics have been computed from the time series for the profile measurements according to standard procedures. All results have been corrected for the spatial integration due to the finite size of the measurement volumes with the methodology described in Durst, Jovanovic & Sender (1993). We have computed statistical errors for various radial positions following Lumley & Panofsky (1964). These are shown as error bars in the resulting figures of §7. The estimated relative error for the mean velocity is about 0.4%, and 1.2% for the root-mean-square.

The power spectra have been computed as follows. The observed time series, which consisted of approximately 196 000 samples distributed in time according to a Poisson random distribution, were re-sampled at equidistant times using linear interpolation between the measured data with the re-sampling frequency equal to the mean data rate of the measurement (f_{dr}). The re-sampled time series were then divided into 186 (± 4) half-overlapping blocks each containing 2048 data points. For each of these blocks, the power spectrum was computed using a FFT and a Bartlett window. The power spectra presented in the figures to follow have been obtained by averaging the spectra of the blocks.

7. Results

In this section we present the results obtained from the DNS with the polymer models described in §§3 and 4 and we compare them with our LDV results. All numerical Newtonian data in this section have been computed from data fields obtained by Eggels (1994). We stress that the comparison between the numerical and the laboratory results can be only a qualitative one, because apart from the rather (over)simplified constitutive equations used in the DNS, the Reynolds number for the DNS and LDV measurements is different. In den Toonder (1995) it is for instance shown that for the Newtonian data we already observe differences between the laboratory and numerical results, due to the difference in Reynolds number. In the simulations, a low Reynolds number must be chosen due to computational limitations, while in the experiments Re could not be chosen too low, because as mentioned above this resulted in negligible drag reduction.

7.1. The viscous anisotropic model (VA)

7.1.1. Flow rate

The time evolution of the flow rate Q^* is depicted in figure 5 for the viscous anisotropic (VA) model. Q^* at $t^* = 0$ corresponds to the flow of the solvent. Note

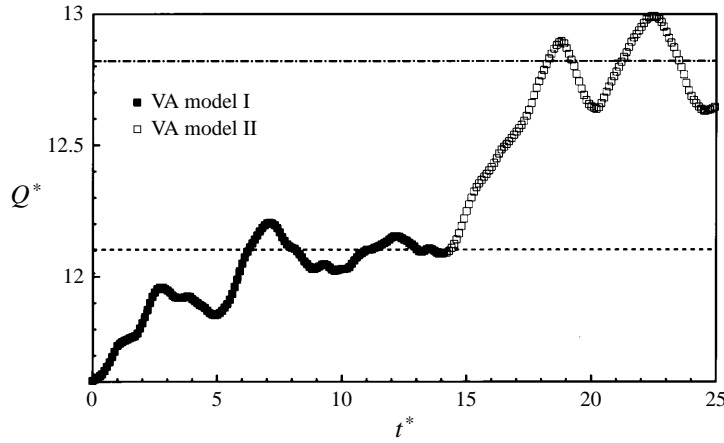


FIGURE 5. Evolution of the flow rate for the viscous anisotropic model. At $t^* = 0$ the polymer model is turned on in a Newtonian flow field. The dashed line indicates the mean value of Q^* between $t^* = 10$ and 14 (model I, for which $\mu_2^* = 0.033$). The dotted-dashed line indicates the same quantity between $t^* = 20.2$ and 24.5 (model II, for which $\mu_2^* = 0.075$).

that the pressure gradient is kept constant in our DNS so that a drag reduction will appear as an increase in flow rate. From $t^* = 0$ to 14, the non-Newtonian parameter μ_2^* has been taken to be 0.033 (i.e. VA model I); from $t^* = 14$ to 25, $\mu_2^* = 0.075$ (VA model II), see (5.3). From figure 5 it is clear that the viscous anisotropic fluid model results in a drag reduction. The fluctuations still visible for model I between $t^* = 10$ and 14 are of a statistical nature. The magnitude of these fluctuations is comparable to that found in the Newtonian simulations of Eggels *et al.* (1994) in the steady-state regime (see also Eggels 1994). The fluctuations in the simulation of model II between $t^* = 19$ and 25 remain large and we may doubt whether a steady state has yet been reached at $t^* = 25$. However, due to lack of computing time, the simulation could not be continued after $t^* = 25$. Nevertheless, from the statistics computed from model II tendencies that follow from increasing μ_2^* in the VA model can be clearly distinguished, as we will see later in this section. The dashed line in figure 5 indicates the mean value of Q^* in the time interval between $t^* = 10$ and 14, which is 12.1 (i.e. for model I). The dotted-dashed line indicates the same quantity for model II, i.e. averaged between $t^* = 20.2$ and 24.5, and it equals 12.8. The value of the drag reduction obtained, defined by (6.2), is thus $DR = 4.1\%$ for model I and $DR = 9.5\%$ for model II. The drag reduction for model I is still small when compared to values that are obtained in experiments; however, it is an order of magnitude larger than DR obtained with the model used in den Toonder *et al.* (1995b). In that study only viscous effects but no anisotropy is taken into account and the increase of the extensional viscosity is the same as in VA model I. Increasing μ_2^* such that the uniaxial extensional viscosity of the VA model is doubled, while the biaxial extensional viscosity is increased by a factor 13/8 (model II, see §3), more than doubles the drag reduction. This clearly suggests that anisotropy introduced in the stress-deformation relation is important for drag reduction.

7.1.2. Mean velocity profile

In figure 6(a) we illustrate the non-dimensional mean axial velocity profile as computed with the VA model as a function of wall distance, scaled with inner variables: $y^+ = yu_c/\nu$. The centre of the pipe lies at $y^+ = 180$. In this figure we also

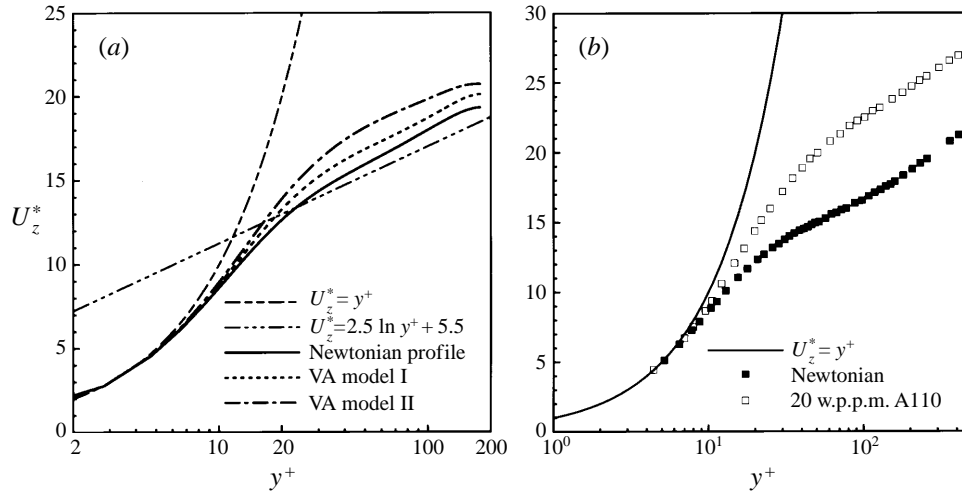


FIGURE 6. Mean axial velocity (a) for the viscous anisotropic model (DNS), and (b) as measured with LDV. The centre of the pipe is at $y^+ = 180$ for the DNS, and at $y^+ \approx 520$ for the LDV.

depict the functions which are generally believed to describe the mean axial velocity profile of turbulent wall flows of Newtonian fluids:

$$U_z^+ = y^+ \quad \text{if} \quad 0 < y^+ < 5, \quad (7.1)$$

$$U_z^+ = A \ln y^+ + B \quad \text{if} \quad y^+ > 30, \quad (7.2)$$

with $A = 2.5$ and $B = 5.5$, as recommended by Kim, Moin & Moser (1987). The region $y^+ < 5$ is called the viscous sublayer, $y^+ > 30$ the logarithmic layer. The inner region where $5 < y^+ < 30$ is the so-called buffer layer. The Newtonian data, which were obtained in a DNS by Eggels *et al.* (1994), do not follow the logarithmic law (7.2). This is due to the low Reynolds number of the flow, as has been confirmed by experiments at the same Reynolds number (den Toonder 1995; Eggels *et al.* 1994). Figure 6(a) shows that the computed profiles obtained with the VA model follow the Newtonian data up to $y^+ = 5$. In the region above $y^+ = 30$, the profile is shifted upward with an approximately parallel displacement for VA model I. In the case of model II, the shift is larger which is consistent with the larger drag reduction, but not quite parallel. This might be because the computation has not completely stabilized to a stationary flow. Figure 6(b) shows the result for the LDV measurements. Here the buffer layer is thickened, which causes an upward shift of the logarithmic profile. However, this shift is not quite parallel to the Newtonian data. The fact that we refer here to a parallel shift of the velocity profile goes back to experiments in the past, which assumed that the slope of the logarithmic profile is the same for water and drag-reduced flows (probably inspired by Virk's elastic sublayer model, see Virk 1975). However, careful inspection of recent measurements, such as those of Pinho & Whitelaw (1990) (pipe flow), Harder & Tiederman (1991) (channel flow) and Wei & Willmarth (1992) (channel flow), shows that the slope actually is somewhat increased for polymer solutions and this is confirmed by our experiments. This result, along with the fact that in the computations the Reynolds number is too low for a well-defined logarithmic region to exist, means that the (non-) parallelness of the velocity shift should not be used as a criterion to judge our simulation results.

Nevertheless, comparison of figures 6(a) and 6(b) shows that the general behaviour

of the mean velocity profile obtained with the VA models is correct, i.e. no change in the viscous sublayer, a thickening of the buffer layer and a corresponding offset of the logarithmic region, resulting in an increase of the velocity profile in the central region.

7.1.3. *R.m.s. statistics*

Figures 7(a), 7(c) and 7(e) give the non-dimensional root-mean-square (r.m.s.) profiles of the axial, radial and circumferential velocity fluctuations respectively for both VA simulations.

As can be seen in figure 7(a), the peak of the axial r.m.s. profile is shifted away from the wall to a higher y^+ value, and the magnitude of the peak is increased. This behaviour is stronger for model II, with the larger drag reduction. Overall there is good qualitative agreement with the measured results shown in figure 7(b), except that in the simulations we do not find the decrease in r.m.s. (u_z^*) that is present in the experiments close to the wall, i.e. below $y^+ = 10$. Furthermore, in the centre of the pipe, the r.m.s. of the axial velocity fluctuations for the VA models is decreased somewhat, which is also not confirmed by the experiments shown in figure 7(b). However, such decrease has been found in the measurements of Rudd (1972) and Pinho & Whitelaw (1990), and less significantly in the results of Wei & Willmarth (1992).

In accordance with the experimental data, figure 7(c) shows a decrease of the radial r.m.s. velocity over almost the entire pipe cross-section. In addition we observe a shift away from the wall of the peak of this profile. In the centre, model I shows a slight decrease in r.m.s. (u_r^*) compared to the Newtonian data. VA model II leads to no change in the pipe centre, which is more in line with the LDV data of figure 7(d). Moreover, the data in figure 7(d) indicate that the measurements close to the wall are not reliable and probably strongly influenced by measurement errors. These errors cannot be explained by the statistical inaccuracies and are due to other error sources such as reflections by the pipe wall which disturb the LDV signals (see also den Toonder & Nieuwstadt 1996). The vertical laser beam pair, that measures the radial velocity component, is most sensitive to such disturbances.

The circumferential r.m.s. (figure 7e), which is only available from our DNS, is smaller everywhere in the pipe than the Newtonian value, as confirmed by the measurements of Pinho & Whitelaw (1990).

The most important conclusion from these simulation results is that the VA models produce the correct tendency for the change in turbulence intensities, i.e. an enhancement in the axial direction and a suppression in the radial and circumferential directions. This effect, which implies that the turbulence structure is modified rather than suppressed, has not been found for the extensional viscosity model used in den Toonder *et al.* (1995b). Also the shift away from the wall of the peak values seems to be correctly simulated by the VA models. Consequently, we consider this a strong indication that anisotropy of the stress is essential in the effect of polymers on the flow.

7.1.4. *Higher-order statistics*

The higher-order turbulence statistics obtained from the DNS using the VA models and from the LDV experiments are depicted in figures 8 and 9.

The change in the axial skewness profile given in figure 8(a) is very similar to the behaviour measured with LDV (figure 8b). There is a slight increase in S_z in the region below $y^+ = 20$, and a clear decrease around $y^+ = 100$.

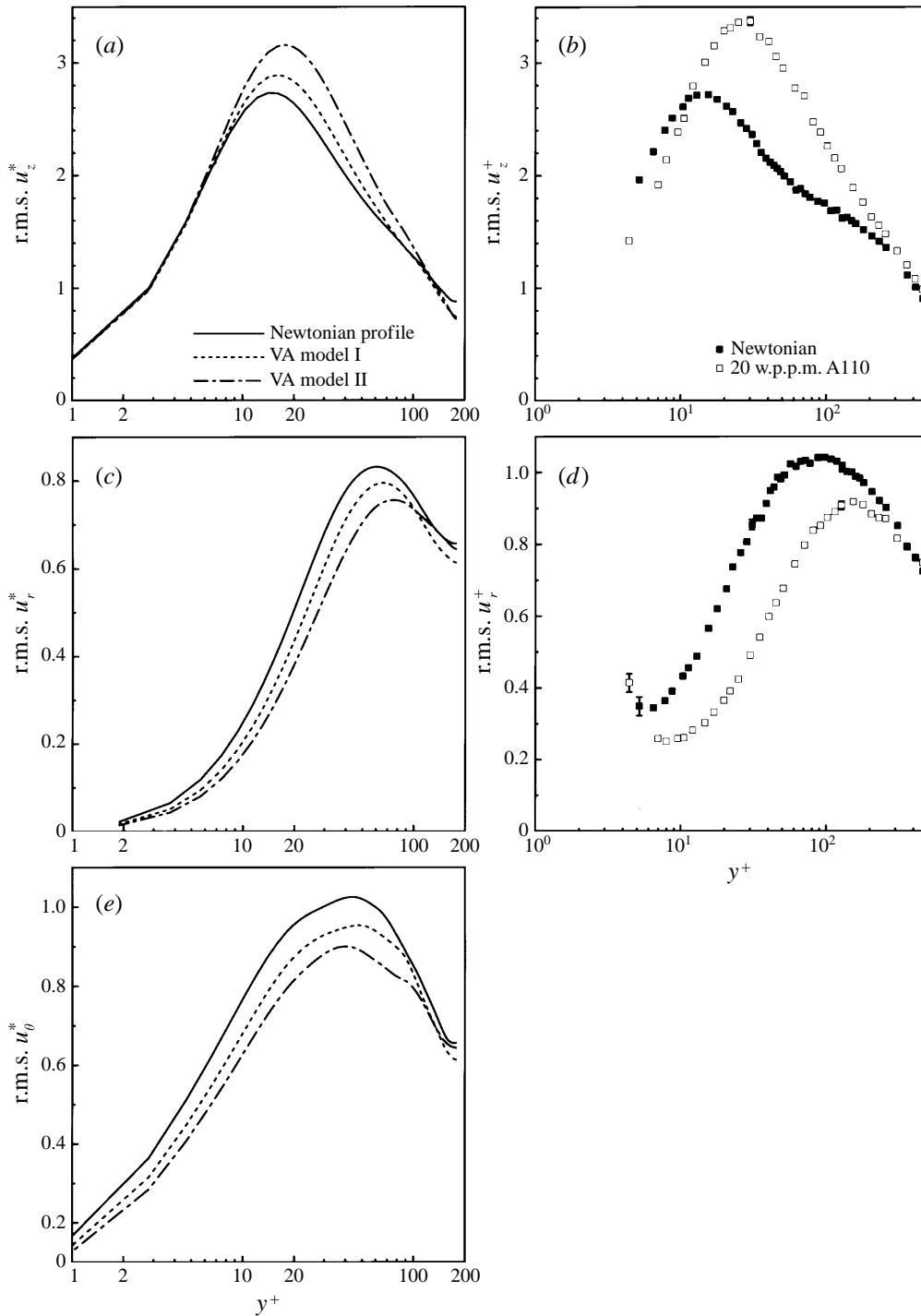


FIGURE 7. R.m.s. profiles: (a) axial profiles for the VA models (DNS); (b) axial profiles measured with LDV; (c) radial profiles for the VA models (DNS); (d) radial profiles measured with LDV; (e) circumferential profiles for the VA models (DNS). The centre of the pipe is at $y^+ = 180$ for the DNS, and at $y^+ \approx 520$ for the LDV.

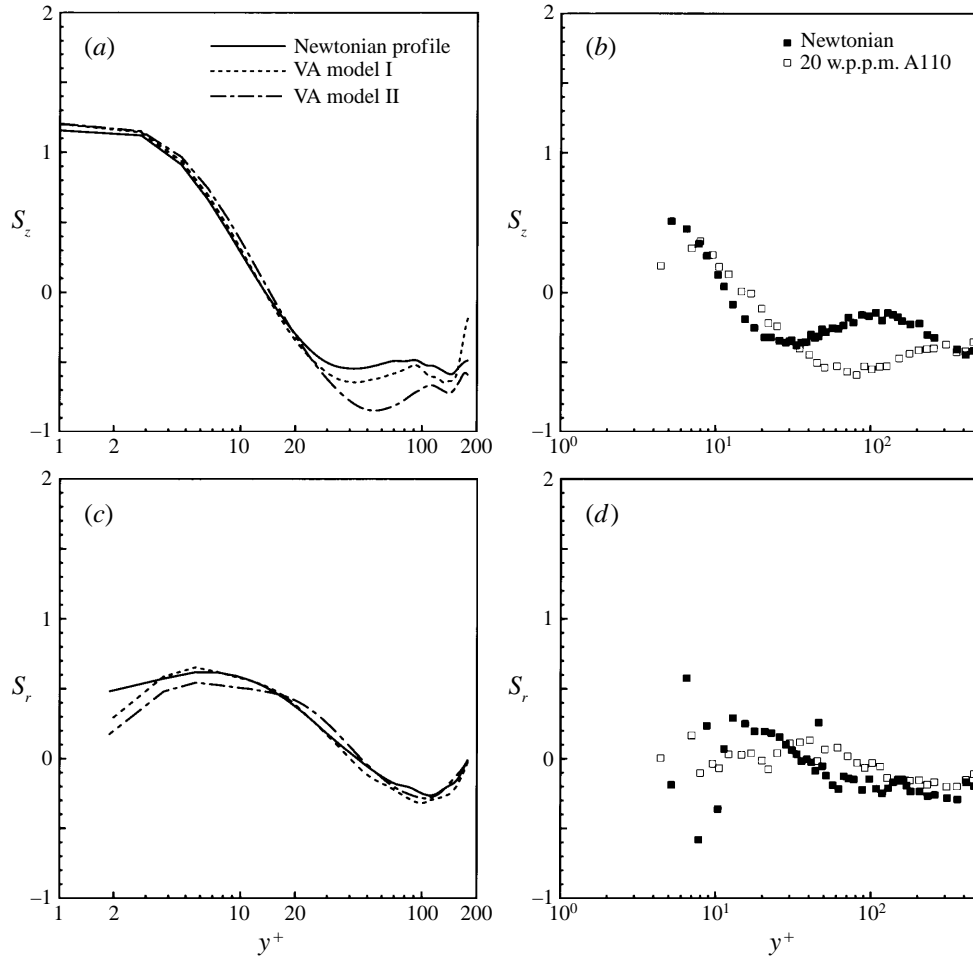


FIGURE 8. Skewness profiles: (a) axial profiles for the VA models (DNS); (b) axial profiles measured with LDV; (c) radial profiles for the VA models (DNS); (d) radial profiles measured with LDV.

Figure 8(c) shows that the radial skewness S_r is not influenced much by the VA model. This is confirmed by the measurements in figure 8(d), which also shows large scatter below $y^+ = 10$, for the reasons discussed in connection with the r.m.s. values near the wall.

The VA model also seems to give the correct tendency for the axial flatness factor F_z , as follows from comparing figures 9(a) and 9(b). With respect to the minimum value, there is a slight shift away from the wall. Around $y^+ = 100$ we find a small increase. The somewhat odd behaviour of the computed F_z close to the centreline is probably due to the lack of sufficient independent realizations in this area to reliably compute F_z .

The radial flatness factor however, shows a large change in behaviour resulting from the VA model: the value of F_r close to the wall is significantly increased. This cannot be confirmed unequivocally by our LDV measurements. Although figure 9(d) seems to indicate a decrease in F_r below $y^+ = 10$, we found in other LDV measurements increases of this quantity (see den Toonder 1995). Moreover, we already have seen above that the radial turbulence statistics are considerably influenced by measurement

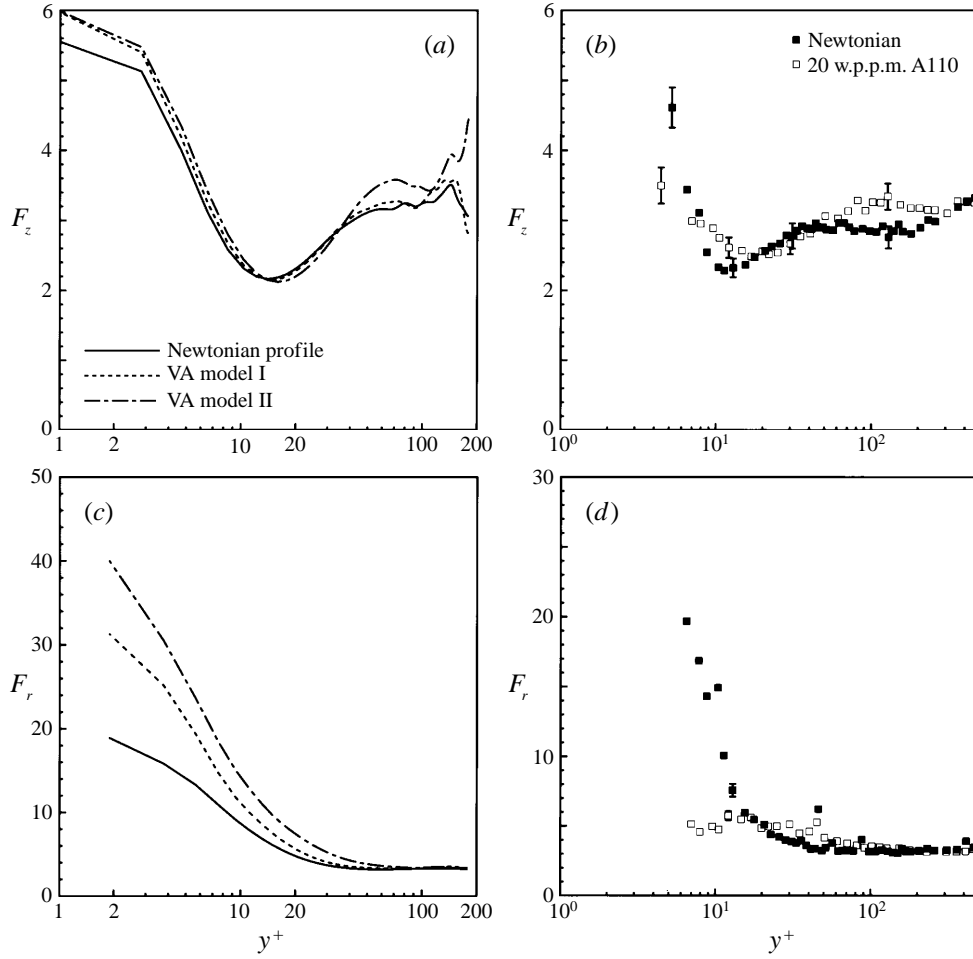


FIGURE 9. Flatness profiles: (a) axial profiles for the VA models (DNS); (b) axial profiles measured with LDV; (c) radial profiles for the VA models (DNS); (d) radial profiles measured with LDV.

noise very close to the wall, and this may explain the large differences found between various experiments. It is also shown in Xu *et al.* (1996) that it is very difficult to measure the radial flatness factor correctly near the wall. Due to these uncertainties, confirmation of the effects on F_r due to the VA model very close to the wall is not yet available.

7.1.5. Stresses

The turbulent shear stress (or ‘Reynolds stress’) τ_T^* is defined as

$$\tau_T^* = \overline{(u_z^* - U_z^*)(u_r^* - U_r^*)}. \quad (7.3)$$

This quantity is depicted in figure 10. For the DNS results, the peak of the profile is again shifted somewhat toward a higher y^+ value, while its magnitude is decreased a little in comparison with the turbulent stress in a Newtonian pipe flow. The change is larger for model II than for model I. This behaviour for τ_T^* is completely analogous with the LDV results depicted in figure 10(b).

The DNS data allow us to calculate the various contributions to the shear stress.

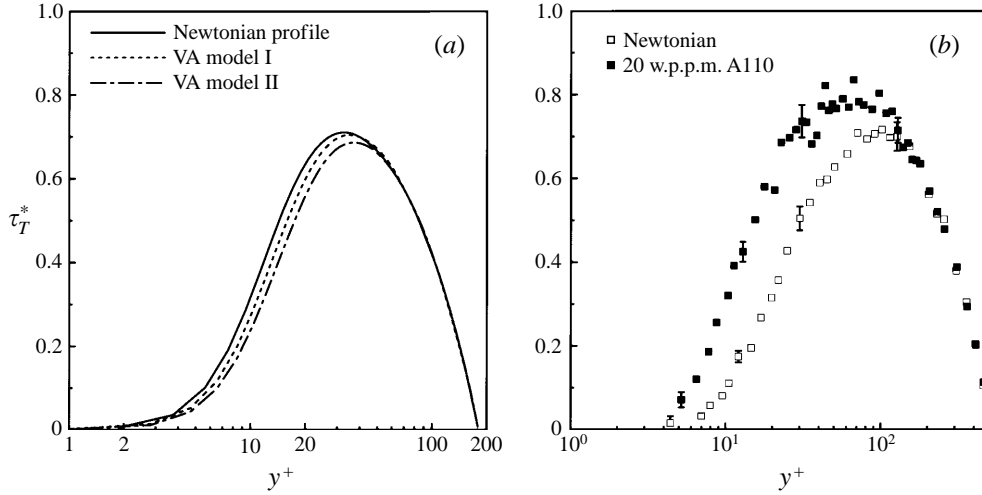


FIGURE 10. Turbulent shear stress (a) for the VA models (DNS), and (b) measured with LDV.

These are illustrated in figures 11(a) and 11(c) for both VA models. The viscous shear stress τ_V^* is defined as

$$\tau_V^* = -\frac{1}{Re_\tau} \left(\frac{\partial u_z^*}{\partial r^*} + \frac{\partial u_r^*}{\partial z^*} \right). \quad (7.4)$$

The components of the ‘polymeric’ stress tensor for the VA models are defined as:

$$\tau_{P,ij}^* = -\mu_2^* (\mathbf{u}^* \cdot \mathbf{D}^* \cdot \mathbf{u}^*) u_i^* u_j^*. \quad (7.5)$$

To obtain the polymer shear stress τ_p^* , i is set equal to the radial coordinate direction r and j to the axial direction z .

For fully developed turbulent pipe flow, the sum of the shear stresses must obey the following balance:

$$2 \frac{r}{D} = \tau_T^* + \tau_V^* + \tau_p^*. \quad (7.6)$$

From figures 11(a) and 11(c) it can be seen that the computed stresses indeed follow this relation fairly well.

For model II, this seems to be in contradiction with our earlier statement of the flow not having reached a steady state in view of the large fluctuations in Q^* present in the simulation at $t^* = 25$ (see figure 5). However, in the averaging procedure we have integrated over exactly one period of this large fluctuation (i.e. between $t^* = 20.2$ and 24.5), so that its effect is probably cancelled out. Therefore, we still believe that the simulation of model II has not strictly reached a steady state, although figure 11(c) suggests otherwise. For model I, no special averaging period was chosen, and the magnitude of the fluctuations in Q^* for this case, along with figure 11(a), indicates that this simulation indeed is close to a steady-state situation. This is consistent with our suggestion that the fluctuations of the flow rate between $t^* = 10$ and $t^* = 14$ in figure 5 are mainly due to the turbulence and not to a residual numerical effect.

Figures 11(a) and 11(c) show that the contribution of τ_p^* to the total shear stress is very small. It means that in our VA simulations no so-called ‘Reynolds stress deficit’ appears (which implies a significant non-Newtonian contribution to the shear stress). The variation in the turbulent shear stress that can be observed in figure 10(a) is completely compensated by viscous effects. In contrast, we have found a Reynolds

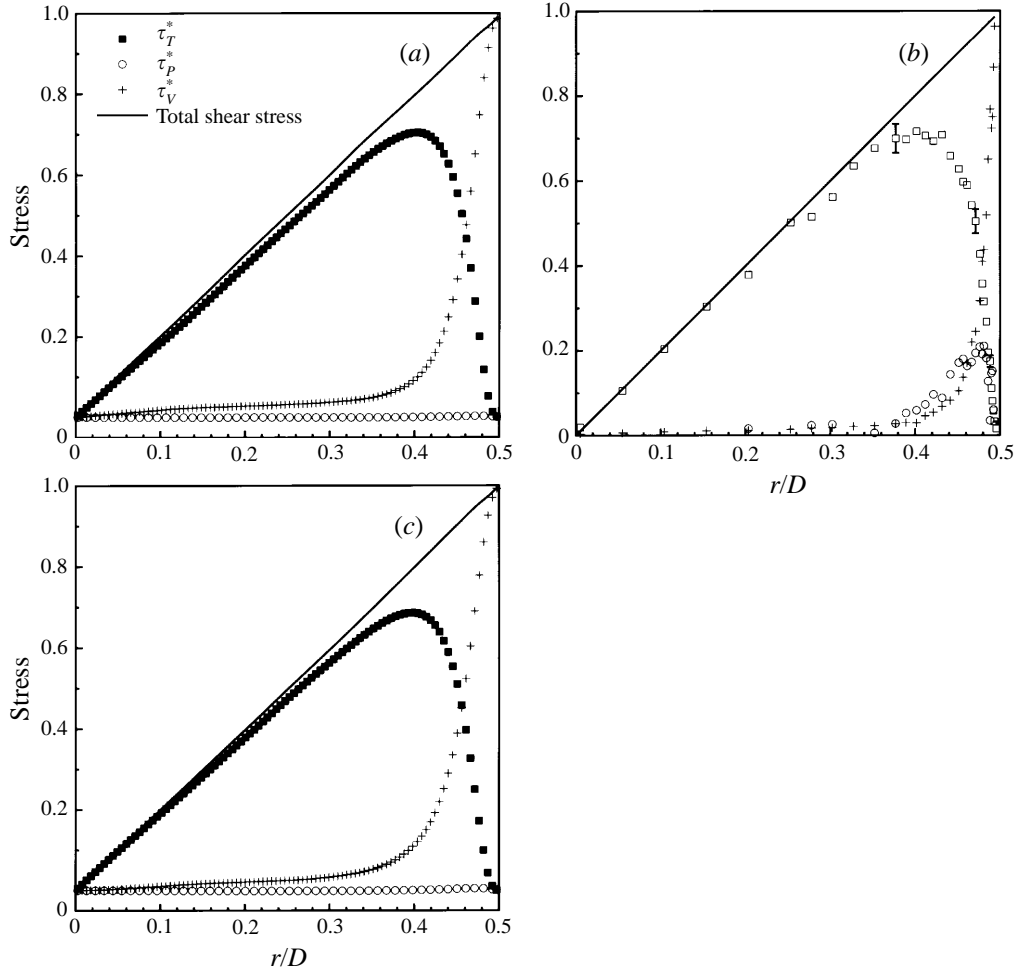


FIGURE 11. Shear stress profiles: (a) VA model I (DNS); (b) LDV measurement, polymer solution; (c) VA model II (DNS).

stress deficit in our LDV experiments. This is illustrated by figure 11(b), in which we show the various contributions to the shear stress for the drag-reduced flow. The turbulent shear stress, τ_T^+ , was measured directly and the viscous shear stress τ_V^+ was computed from the measured mean velocity profile. The polymer shear stress τ_P^+ is determined from the stress balance (7.6) by substituting the measured τ_T^+ and τ_V^+ . It turns out that the polymers make a significant contribution to the shear stress outside the core region of the pipe, particularly in the buffer layer. The majority of experimental papers on polymeric drag reduction also report a Reynolds stress deficit, although also some exceptions exist. Harder & Tiederman (1991) for example have used a very dilute polymer solution that gave a drag reduction but no Reynolds stress deficit.

To elaborate the additional stresses due to the polymer model, we show in figure 12(a) the profiles of the largest components and in figure 12(b) the smaller components of the polymeric stress tensor for the VA model II. These are defined according to (7.5). From figure 12(a) it is clear that the zz component has the largest

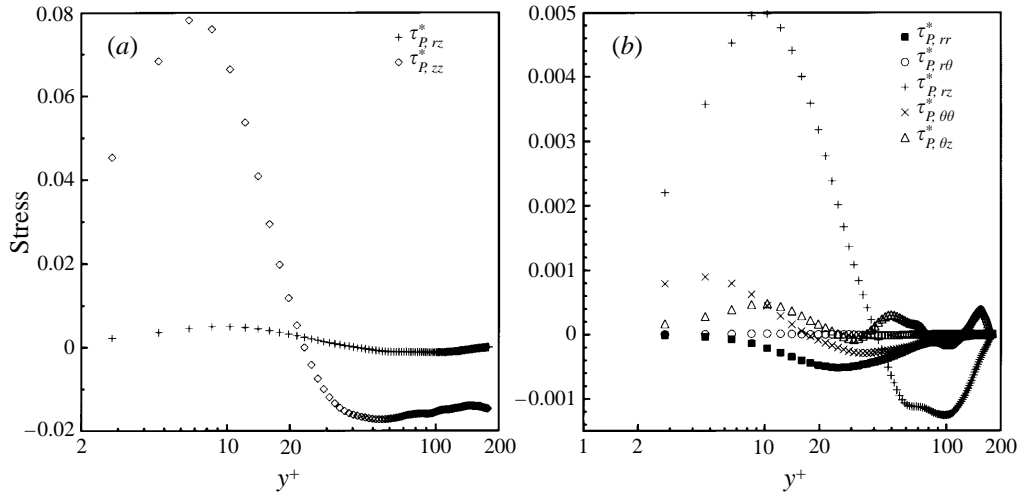


FIGURE 12. Profiles of (a) the largest components, and (b) the smallest components, of the polymeric stress tensor for VA model II (DNS).

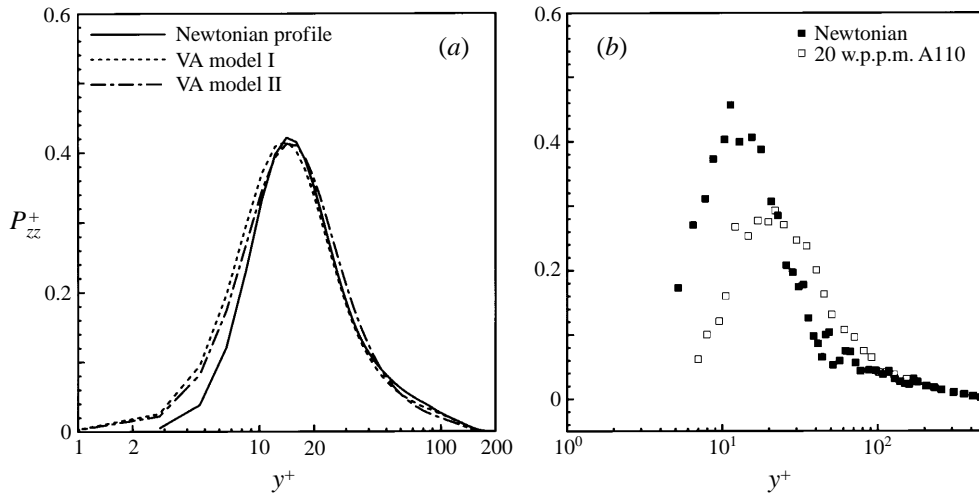


FIGURE 13. Turbulent energy production: (a) for the VA models (DNS), and (b) measured with LDV.

value. This is not too surprising, because in the simulations the anisotropic direction was chosen along the local instantaneous velocity, and in the mean the orientation of \mathbf{u}^* is in the axial or z -direction. Furthermore, the $\tau_{P,zz}^*$ profile peaks around $y^+ = 10$, which is in the buffer layer. Also, the rz component seems to have a significant value when compared with the other components in figure 12(b). However, the rz component is the polymer shear stress already shown in figure 11(c) where we have argued that its contribution to the total shear stress is minimal. According to figure 12(b), all other polymeric stress components are quite small over the entire pipe cross-section. Hence it seems that the changes in the flow leading to the drag reduction are mainly due to the additional normal stress in the axial direction, and to a much smaller extent to the additional shear stress.

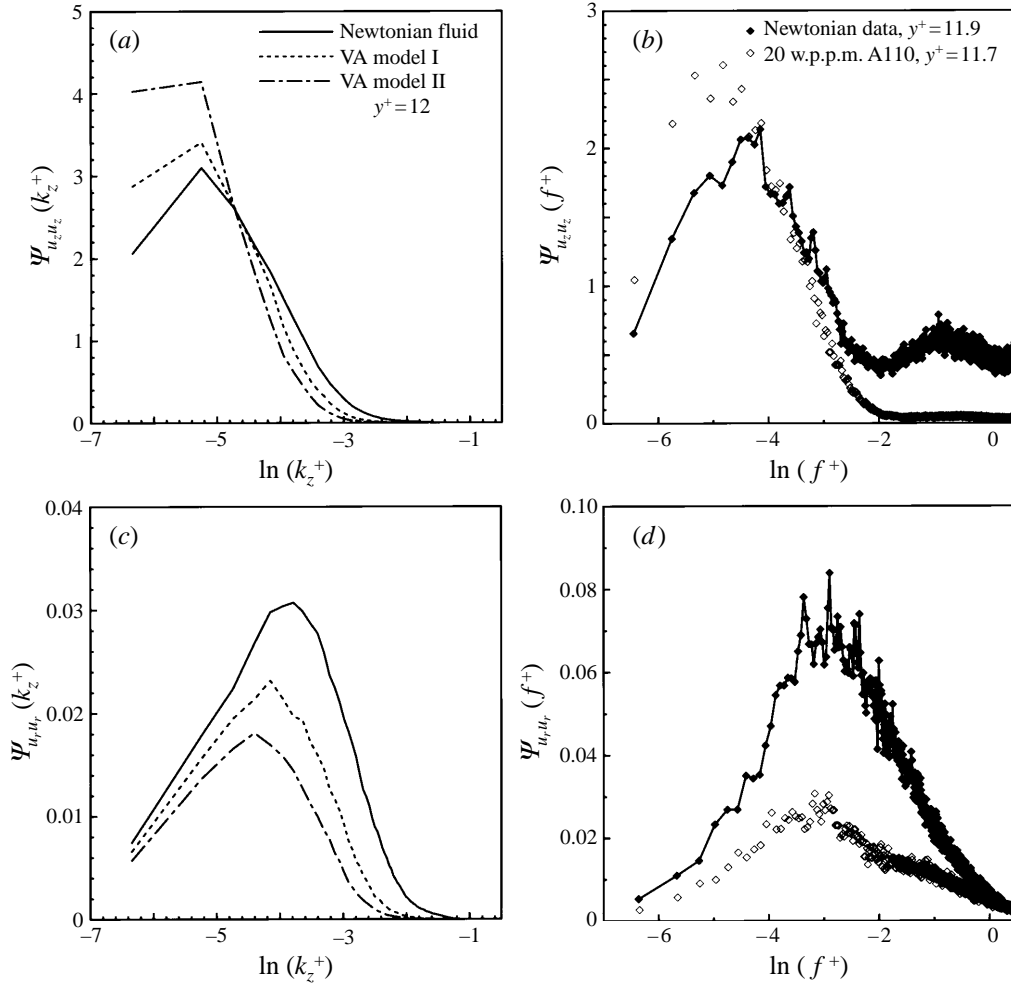


FIGURE 14. Power spectra at $y^+ \approx 12$: (a) axial component, VA models (DNS); (b) axial component, measured with LDV; (c) radial component, VA models (DNS); (d) radial component, measured with LDV.

7.1.6. Turbulent energy production

The turbulent energy production P_{zz} is defined as

$$P_{zz} = -2\tau_T \frac{dU_z}{dr}. \quad (7.7)$$

The influence of the VA model on the turbulent energy production P_{zz}^+ can be observed in figure 13(a). For $y^+ > 10$, there is almost no change with respect to the Newtonian profile. For run II a very slight shift away from the wall and a minimal decrease of the peak value may be noticed; however the clear change found in the LDV measurements of figure 13(b), is not confirmed by the simulations. Also, the increase of P_{zz}^+ in the region $y^+ < 10$ found in the DNS results of figure 13(a) cannot be confirmed by the data of figure 13(b), partly due to the lack of measurement points.

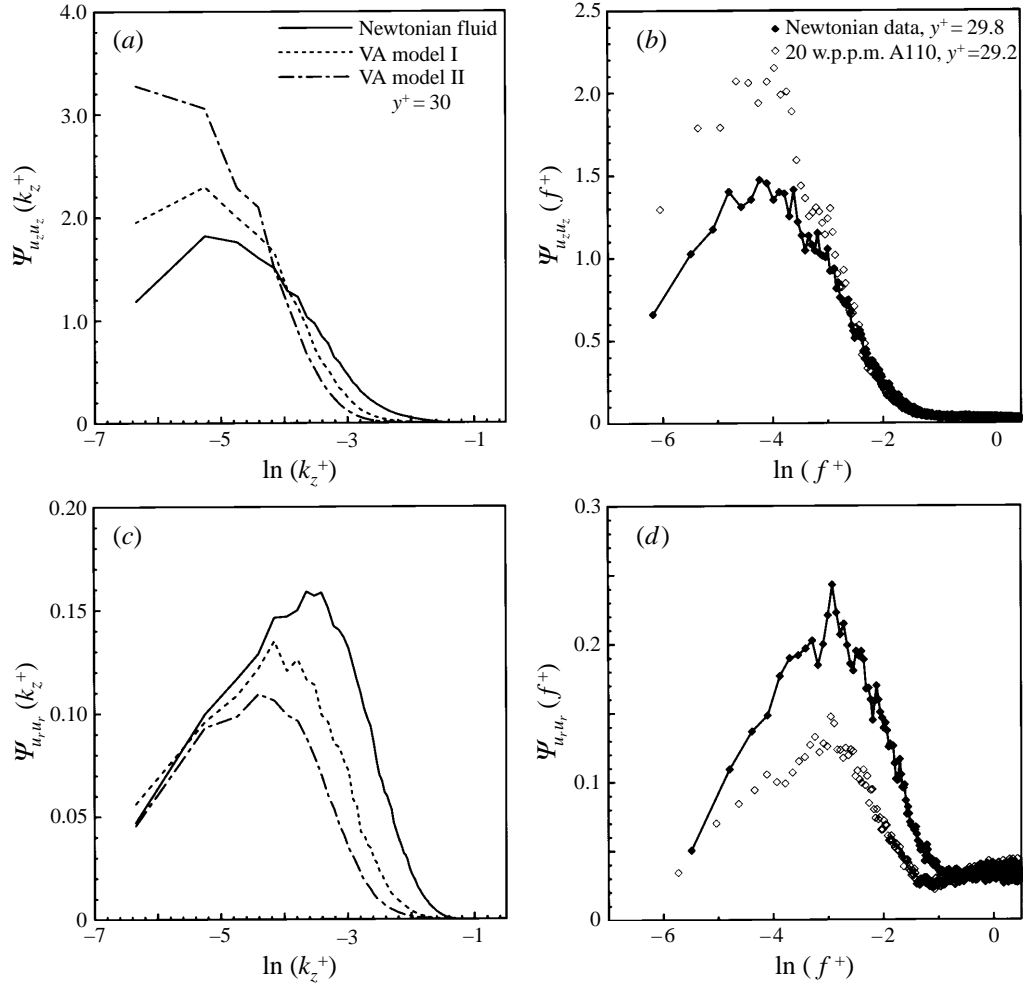


FIGURE 15. Power spectra at $y^+ \approx 30$: (a) axial component, VA models (DNS); (b) axial component, measured with LDV; (c) radial component, VA models (DNS); (d) radial component, measured with LDV.

7.1.7. Power spectra

One-dimensional power spectra have been computed at $y^+ = 12, 30$ and 125 . These spectra, shown in figures 14–16 along with the LDV results, are plotted in the format introduced by Perry & Abell (1975) that was also used in the experimental paper of Wei & Willmarth (1992). The abscissa is the logarithm of the dimensionless wavenumber in the z -direction, $k_z^+ = k_z \nu / u_\tau$. The ordinate, $\Psi_{u_x u_x}(k_z^+)$, is defined so that the area beneath a semi-logarithmic plot of $\Psi_{u_x u_x}(k_z^+)$ is proportional to the mean square of the fluctuating signal, made dimensionless with u_τ , i.e.

$$\int \Psi_{u_x u_x}(k_z^+) d(\ln k_z^+) = \frac{\overline{u_x u_x}}{u_\tau^2}. \quad (7.8)$$

The relation between $\Psi_{u_x u_x}(k_z^+)$ and the standard one-dimensional spectrum, $\Phi_{u_x u_x}(k_z^+)$, is

$$\Psi_{u_x u_x}(k_z^+) = k_z^+ \Phi_{u_x u_x}(k_z^+). \quad (7.9)$$

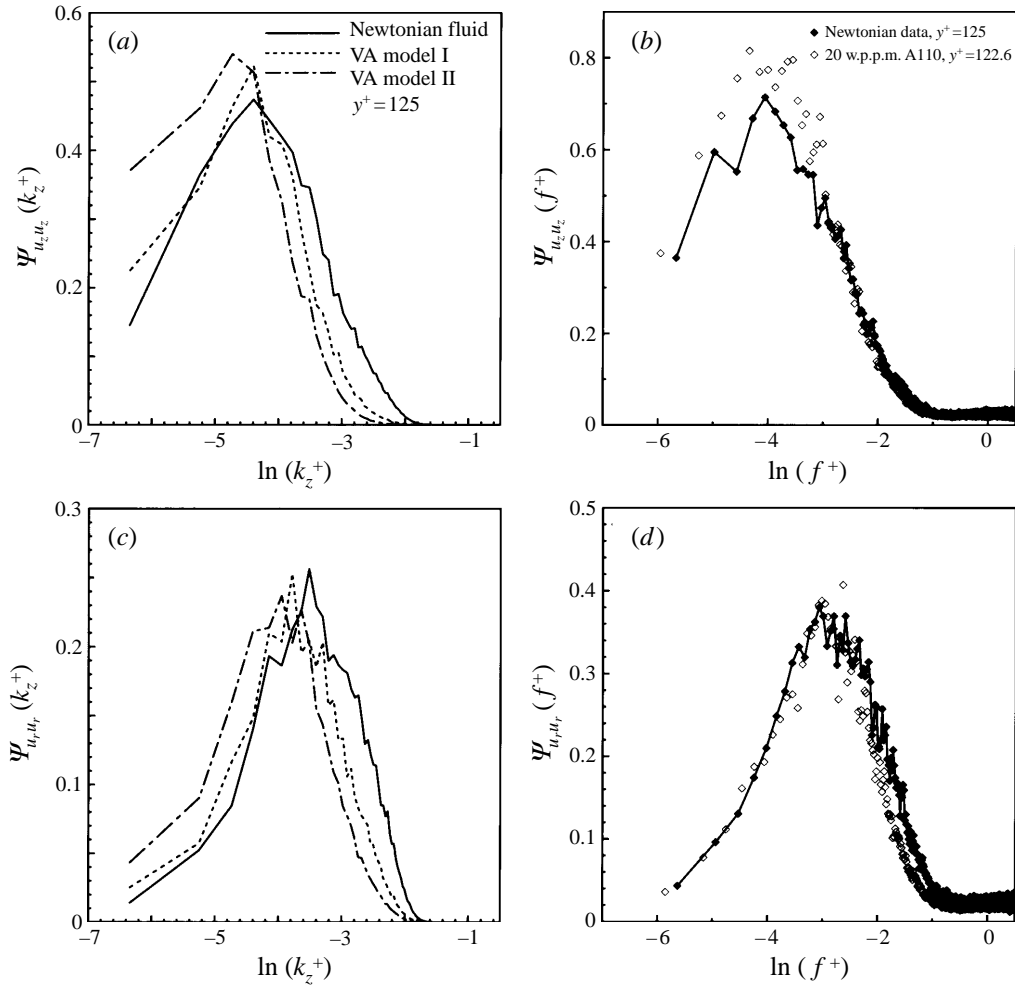


FIGURE 16. Power spectra at $y^+ \approx 125$: (a) axial component, VA models (DNS); (b) axial component, measured with LDV; (c) radial component, VA models (DNS); (d) radial component, measured with LDV.

In the figures for the LDV measurements, we use the frequency f instead of the streamwise wavenumber k_z . Hence, the abscissa is the logarithm of the non-dimensional frequency, $f^+ = f\nu/u_\tau^2$, and the ordinate is $\Psi_{u_z u_z}(f^+)$. The area beneath the semi-logarithmic plot of $\Psi_{u_z u_z}(f^+)$ against f^+ is again proportional to the mean square of the fluctuating signal, made dimensionless with u_τ .

Power spectra of the fluctuating u_z - and u_r -components at $y^+ = 12$ are given in figure 14. The spectrum of the axial component, given in figure 14(a), for the anisotropic model shows a shift of the energy towards smaller wavenumbers in comparison with the Newtonian results. This means that the energy at small scales is decreased, while it is increased at large scales. The same is found in the LDV measurements for the polymer solution, as can be seen in figure 14(b). In this figure, the difference in noise levels, apparent from the value of $\Psi_{u_z u_z}$ at high frequencies, is different for the Newtonian data than for the polymer solution. The reason for this remains unclear, and this effect is not found in the other spectra to be presented later.

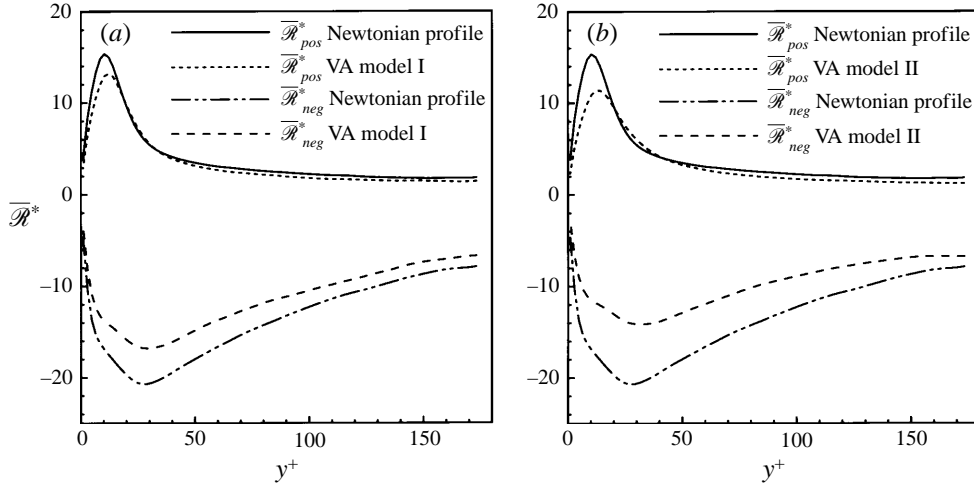


FIGURE 17. Mean elongation parameter: (a) VA model I; (b) VA model II.

Figure 14(c) shows that the turbulent energy of the radial component is suppressed over the entire wavenumber domain, and there is a small shift of the peak in the spectrum towards smaller wavenumbers. The measurements show the same kind of behaviour (see figure 14d), although the suppression of energy is more drastic, which is related to the larger value of drag reduction in the measurements.

The spectra at $y^+ = 30$ (figure 15) exhibit virtually the same characteristics as the spectra at $y^+ = 12$, only here the shift in turbulent energy from small to large scales is even more pronounced. Again, in a qualitative sense the comparison with the LDV measurements shown in figures 15(b) and 15(d) is good, except that the shift in the radial spectrum of the measurements is not as large.

Finally, the spectra at $y^+ = 125$ are shown in figure 16. The axial spectrum of the DNS data is suppressed at high wavenumbers, and increased at the lowest wavenumbers for VA model II, while for model I there is not much change at the small wavenumbers. In the latter case the energy is only somewhat increased in the energy-containing wavenumber region. In the computed radial spectrum (shown in figure 16c) the VA model causes a shift to larger scales of the entire spectrum. The LDV result for the axial spectrum, as shown in figure 16(b), shows reasonable consistency with the computed behaviour although the shift is not as pronounced. The measured radial power spectrum in figure 16(d) shows a decrease in energy at small scales, but there is no clear shift.

7.1.8. Flow structures

Finally, we consider in more detail how the viscous anisotropic stress influences the structure of turbulence in order to find an explanation for the drag-reducing effect of the polymers. To quantify the changes in the turbulence structure, we use the parameter \mathcal{R} , introduced in den Toonder, Kuiken & Nieuwstadt (1996), which is designed to characterize so-called strong flow regions in the turbulence. These are regions in which large stretching (positive or negative) of material elements takes place. The parameter, which is called the ‘elongation parameter’ \mathcal{R} , is defined by

$$\mathcal{R} = -\frac{3\Pi_D}{\Pi_D}, \quad (7.10)$$

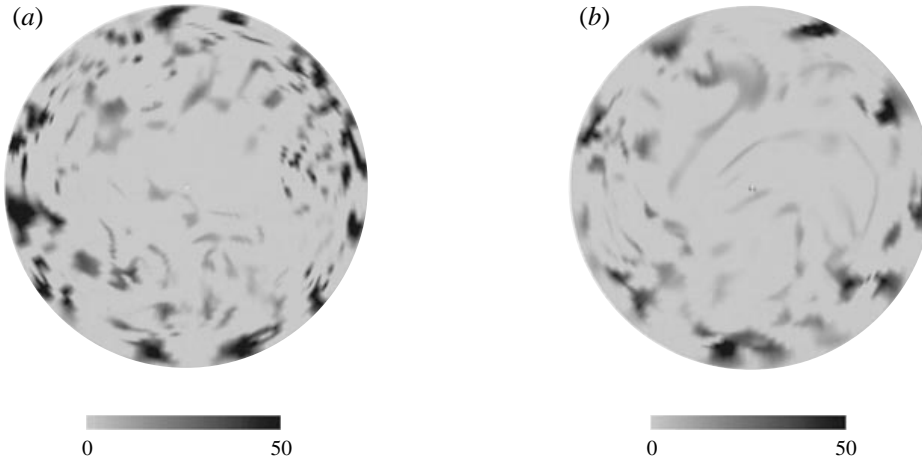


FIGURE 18. Instantaneous fields of \mathcal{R}^* . Cross-section perpendicular to the flow. In the lightest area: $\mathcal{R}^* \leq 0$; in the darkest area: $\mathcal{R}^* \geq 50$. (a) $t^* = 0$ (Newtonian situation); (b) $t^* = 24.5$ (VA model II).

where II_D and III_D are the second and the third invariants of the rate-of strain tensor \mathbf{D} , respectively. It is shown in den Toonder *et al.* (1996) that in regions where \mathcal{R} is positive and large, there is a strong positive stretching deformation in the flow, whereas in regions where \mathcal{R} is negative and large, there is a strong negative stretching, i.e. compression (or squeezing) deformation. Moreover, it is shown that regions with large negative \mathcal{R} values correspond to regions with large positive enstrophy production. We note that in two dimensions better parameters than \mathcal{R} have been proposed in the literature, e.g. Lumley (1972), but in our three-dimensional case \mathcal{R} is quite suitable.

In figure 17 we show the mean non-dimensional $\overline{\mathcal{R}^*}$ averaged over all positive values (\mathcal{R}_{pos}^* , positive stretching) and over all negative values (\mathcal{R}_{neg}^* , compression). From these results it can be seen how the deformation characteristics of the flow are changed by our anisotropic VA model. We find that, in the mean, stretching as well as compressing motion of the flow is suppressed by the VA model, but that the suppression of the negative \mathcal{R} is larger and extends over the whole flow. This implies less enstrophy production in the anisotropic fluid. The peak of positive stretching is displaced slightly wall-outward. These effects are larger for model II than for model I.

Figures 18(a) and 18(b) show a cross-section of the pipe in which the instantaneous values of \mathcal{R}^* are shown. Only regions with positive stretching are visualized. The regions in which the largest stretching takes place are dark, and these are predominantly situated in the near-wall buffer region. By comparing both figures, we may conclude that the stretching structures are indeed somewhat suppressed by the VA model.

Figures 19(a) and 19(b) are similar to figures 18(a) and 18(b), but here only negative values of the elongation parameter \mathcal{R}^* are visualized, thus illustrating the regions with the largest compression. Comparison of the two figures confirms that compression is strongly suppressed by the anisotropic model. This is also clear from figures 20(a) and 20(b) in which we also show a picture of the instantaneous negative values of \mathcal{R}^* but now in two cross-sections parallel to the flow.

As mentioned before, regions with large squeezing deformation are directly coupled to enstrophy production. Hence, the observed change in the compression regions by

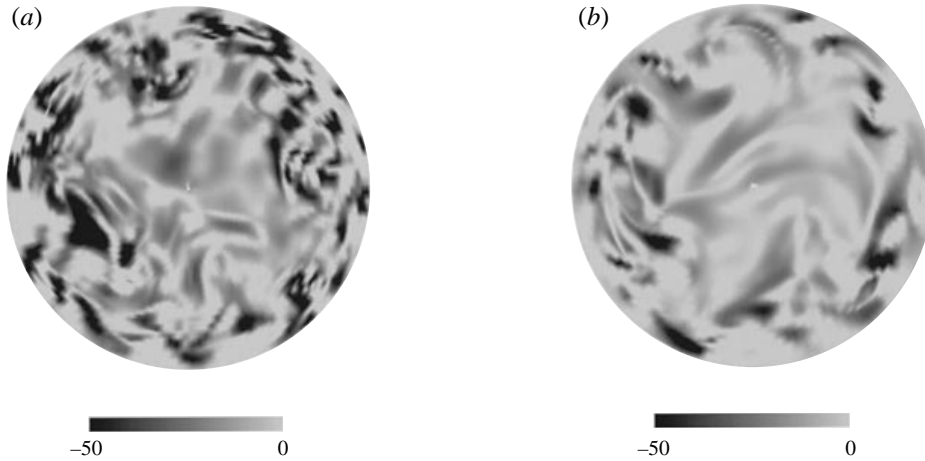


FIGURE 19. As figure 18 but in the lightest area: $\mathcal{R}^* \geq 0$; in the darkest area: $\mathcal{R}^* \leq -50$.

the anisotropic model implies a change in the enstrophy generation. This is confirmed by figure 21, which shows the average of the non-dimensional enstrophy production, defined by

$$P_\epsilon = \boldsymbol{\omega} \cdot \mathbf{D} \cdot \boldsymbol{\omega}, \quad (7.11)$$

in which $\boldsymbol{\omega}$ is the vorticity vector. The anisotropic model causes the value of $\overline{P_\epsilon^*}$ to decrease over the entire pipe cross-section and the decrease is largest in the case of run II. The production of enstrophy is related to vortex stretching, and this process plays a key role in the turbulent energy cascade which is an essential ingredient in the dynamics of turbulent flow (e.g. Tennekes & Lumley 1972). The suppression of the enstrophy production by the anisotropic model thus implies that the energy cascade is hampered. This is consistent with the changes that we have observed in the power spectra where we found a decrease of the small scales with respect to the large scales.

7.2. The viscoelastic anisotropic model (VEA)

In this section we present the results of the DNS of a turbulent pipe flow with the viscoelastic anisotropic (VEA) model presented in §4. The results are compared with the data obtained with model I of the viscous anisotropic (VA) model, which have been discussed in the previous section, and also with the results obtained for the Newtonian model by Eggels *et al.* (1994). In both the VA model I and the VEA model, the parameter μ_2^* was set to 0.033.

7.2.1. Flow rate

The time evolution of the flow rate Q^* is depicted in figure 22, where it should be remembered that u_τ is kept constant in the simulations. As both simulations were initiated from a Newtonian fluid flow, Q^* at $t^* = 0$ corresponds to the flow rate of the solvent. Figure 22 shows clearly that both anisotropic models result in a flow enhancement, or equivalently, in drag reduction. The fluctuations in Q^* visible in figure 22 after $t^* = 10$, are of a statistical nature as we will see later. The solid line in figure 22 indicates the mean value of Q^* in the case of the VA model I in the time interval $t^* = 10$ to 14, which, as we have seen before, is 12.1. The dashed line indicates the same quantity for the VEA model, and it equals 11.7. As a result

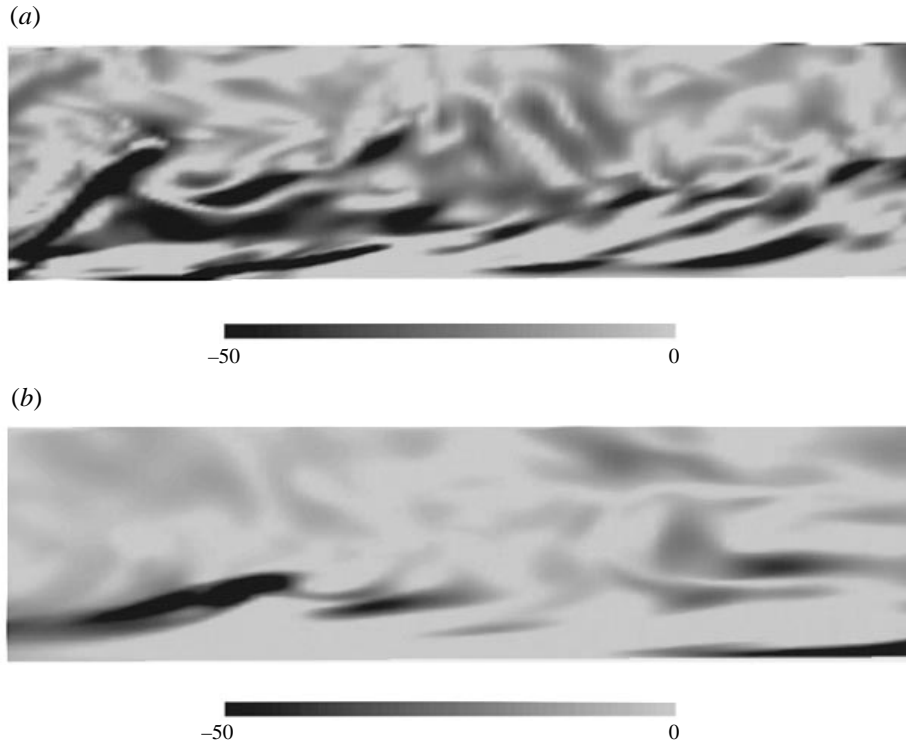


FIGURE 20. Instantaneous field of \mathcal{R}^* . Cross-section parallel to the flow, flow from left to right, bottom of the figure: pipe wall, top of the figure: pipe centre. In the lightest area: $\mathcal{R}^* \geq 0$; in the darkest area: $\mathcal{R}^* \leq -50$. (a) $t^* = 0$ (Newtonian case); (b) $t^* = 24.5$ (VA model II).

we find for the drag reduction defined by (6.2) the value of 4.1% for the viscous case, as also obtained in the previous section, and only 0.7% for the viscoelastic case. Our DNS thus suggests that to induce drag reduction anisotropic viscous effects are more important than anisotropic elastic effects. Indeed, the extension of the viscous anisotropic model with an elastic component reduces the drag-reducing effectiveness considerably. Hence, the viscous anisotropic stresses introduced by the polymer additives seem to be the key ingredient for polymeric drag reduction. This important point will be returned to in our final discussion.

7.2.2. Mean velocity profile

Figure 23 shows the non-dimensional mean axial velocity profile. Both anisotropic profiles follow the Newtonian data up to $y^+ = 5$. In the region above $y^+ = 30$, the viscous profile is shifted upward with an almost parallel displacement, which, as already mentioned in §7.1, is consistent with experimental observations of polymeric drag reduction. The viscoelastic model shows an entirely different behaviour: the profile is affected slightly only around $y^+ = 40$ and remains unchanged with respect to the Newtonian profile at other values of y^+ . This behaviour is clearly not in agreement with experiments.

7.2.3. R.m.s. statistics

Figures 24(a), 24(b) and 24(c) show the profiles of the non-dimensional root-mean-square (r.m.s.) values of the axial, radial and circumferential velocity fluctuations

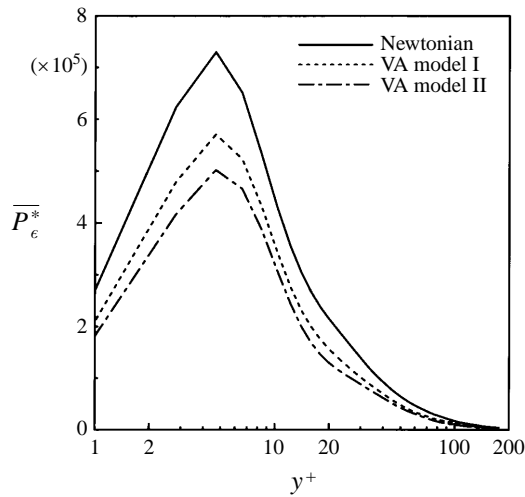


FIGURE 21. Mean entrophy production for the viscous anisotropic models.

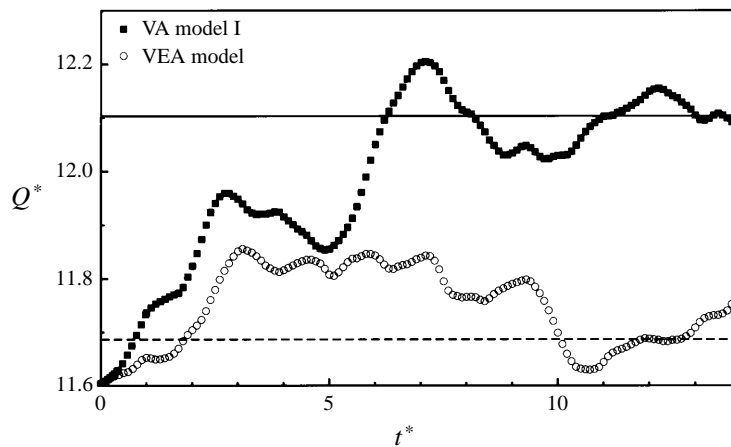


FIGURE 22. Evolution of the flow rate. At $t^* = 0$, the polymer models are turned on in a Newtonian flow field. The solid line indicates the mean value of Q^* between $t^* = 10$ and 14 for the viscous anisotropic model, model I; the dashed line indicates the same quantity for the viscoelastic anisotropic model.

respectively. As can be seen in figure 24(a), the peak of the axial r.m.s. profile is slightly shifted away from the wall to a higher y^+ value, and the magnitude of the peak is increased by both anisotropic models, although the effect for the viscoelastic model is smaller. We have already mentioned in §7.1 that such behaviour is in accordance with experimental data. However, it is clear that this behaviour is suppressed by the elastic effect. In accordance with most experimental data, figure 24(b) shows a decrease of the radial r.m.s. velocity along the entire pipe cross-section for both models, with only slight differences between the two models. The peak of this profile is also shifted away from the wall. The circumferential r.m.s. profile (figure 24c) is decreased everywhere in the pipe with respect to the Newtonian value for both models, as confirmed by measurements of Pinho & Whitelaw (1990). The peak of

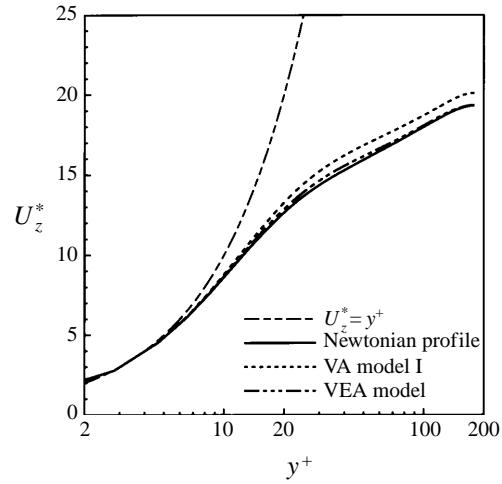


FIGURE 23. Mean axial velocity profiles for VA model I and the VEA model (DNS). The centre of the pipe is at $y^+ = 180$.

this profile, however, is shifted towards the wall by the viscoelastic model, while it is shifted away from the wall by the viscous model.

In general, we see that the r.m.s. profiles for the VA model and the VEA model give the same qualitative behaviour, although the change in the axial r.m.s. is weaker for the VEA model.

7.2.4. Other statistics for the VEA model

In this subsection we summarize the changes in turbulence statistics that we have obtained for the VEA model, other than the mean and the r.m.s.

First, there is not much difference between the VEA model and the VA model I for the skewness and the flatness factors. In any case the small differences observed between the results obtained with both models are not systematic.

Like the VA model I, the VEA model does not generate a Reynolds stress deficit, while the total shear stress follows the linear profile dictated by the shear stress balance (7.6). The latter is an indication that the simulation has reached a steady state at $t^* = 10$.

With respect to the individual components of the polymeric stress tensor for the VEA model, we have found the same kind of behaviour as for the VA models presented in §7.1. The zz component of the polymeric stress makes the largest contribution, while the other components are quite small over the entire pipe cross-section.

The influence of the VEA model on the turbulent energy production and the enstrophy generation is similar to the influence of the VA models shown in figures 13 and 21, respectively, but the changes caused by the VEA model are weaker.

7.2.5. Significance of elasticity

Finally, we consider to what extent the elasticity has played a role in our DNS with the VEA model as compared to purely viscous anisotropic contributions to the stress. To this end, we display in figure 25 the average of the absolute values of the terms in equation (5.5) for F^* , computed from the simulated data with $\mu_2^* = 0.033$ and $\lambda^* = 0.02$. It can be seen that the elastic and the viscous terms are of comparable order of magnitude, the elastic contribution being somewhat smaller. Hence, it may

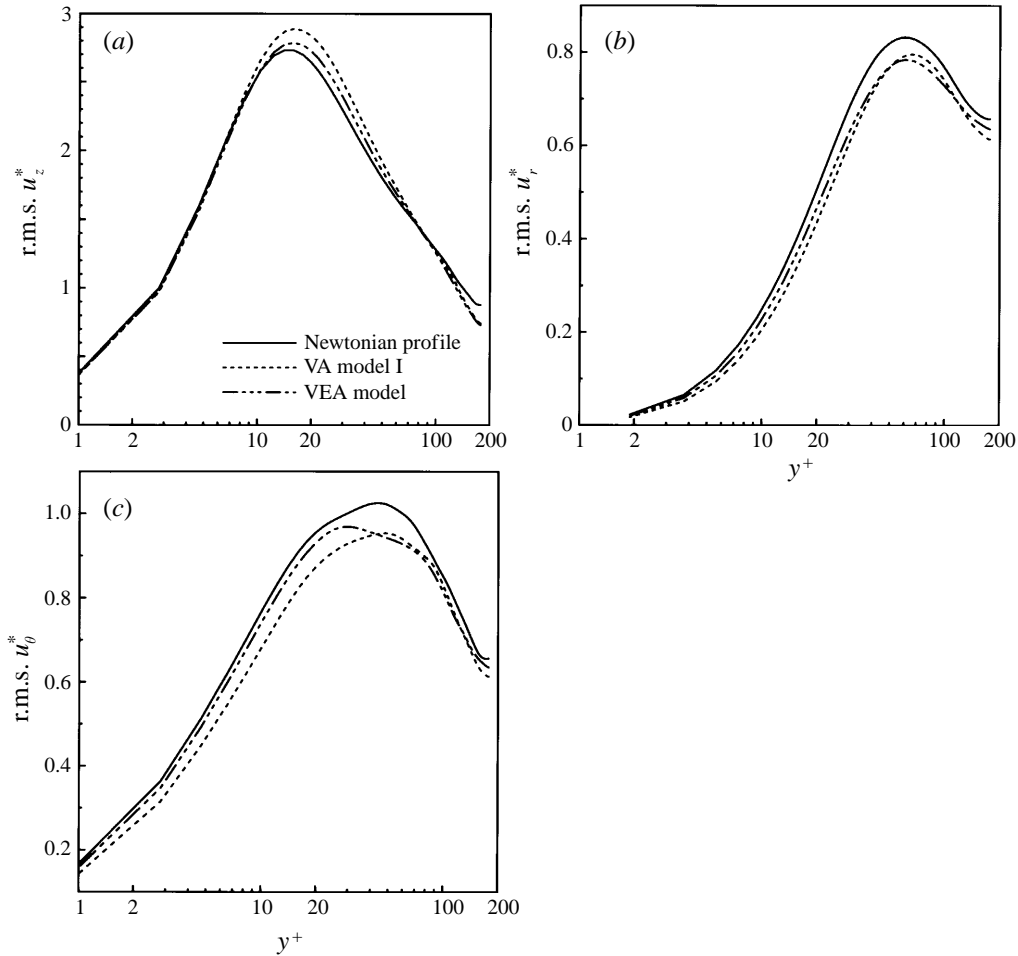


FIGURE 24. R.m.s. profiles for the VEA model and the VA model I: (a) axial component; (b) radial component; (c) circumferential component.

be concluded that the choice of the values for the material constants has resulted in truly overall viscoelastic behaviour, and that the process has not been dominated by either viscous or elastic effects. Therefore, the comments made above with respect to the effect of elasticity on drag reduction seem justified.

8. Conclusions and discussion

Our DNS results support the hypothesis that the key property for drag reduction by polymer additives is related to a purely viscous anisotropic stress introduced by extended polymers. Furthermore, the results suggest that elastic behaviour only reduces the drag-reducing effectiveness. This is in our opinion the main conclusion to be drawn from the present investigation.

Let us also summarize the main points of our study. We have conducted a DNS of turbulent pipe flow in which the effect of polymer additives has been modelled with a simplified constitutive equation which introduces a viscous anisotropic stress. The model, in which the polymers are represented as elongated particles aligned

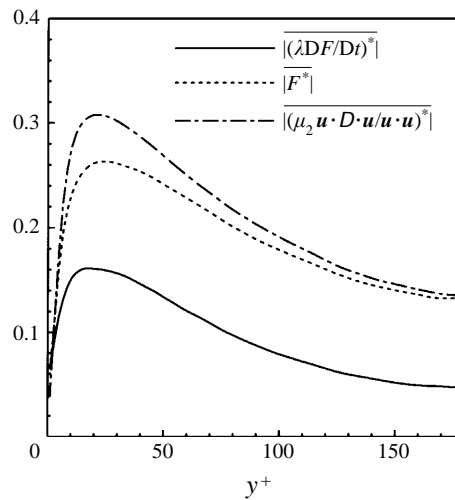


FIGURE 25. The average of the absolute values of the terms in equation (5.4).

with the instantaneous flow vector, should be considered as a simplification, made necessary by computational restrictions. Although in particular our approximation of the particles locally aligned with the flow is strictly not correct in an unsteady flow like turbulence, it seems to be a reasonable first approximation, and thus in our opinion the model captures the essence of viscous anisotropic effects presumably introduced by elongated polymers. The DNS showed a significant drag reduction, which became larger with increase of the non-Newtonian parameter in the model. Based on the computational results we have noticed the following changes between Newtonian and drag-reduced flow.

The buffer layer is thickened for the drag-reduced flow and the logarithmic region has a corresponding offset. The peak of the axial r.m.s. profile is increased and shifted away from the wall, while in the other directions the r.m.s. velocity is decreased. All changes in the higher-order moments are rather small. There is no clear evidence of a Reynolds stress deficit in the DNS. The changes caused by the viscous anisotropic model seem to be mainly due to an additional normal stress in the axial direction. The turbulent energy of the axial velocity is redistributed from small scales to large scales. This change, which shows up in the power spectrum, is largest in the buffer region. The energy of the radial velocity fluctuations is damped over the entire wavenumber domain close to the wall, and the power spectra of this component show a slight shift toward low wavenumbers. It has also been shown that the stretching characteristics of the flow are changed by the viscous anisotropic model, i.e. positive as well as negative stretching deformations are suppressed. Negative stretching, which corresponds to positive enstrophy production, is suppressed more strongly than positive stretching.

Almost all these changes have been confirmed (at least qualitatively) by the results of LDV experiments in a turbulent pipe flow of a dilute polymer solution, which we have also presented in this paper. The exception is the clear Reynolds stress deficit that we find in the measurements and which is lacking in the DNS. This difference probably is due to the small value of the non-Newtonian parameter in our viscous anisotropic model.

To test the hypothesis of de Gennes (1990) that the polymer effects could be described by an elastic modulus and not by a viscosity, and that therefore elasticity is

the key property for drag reduction, we performed another DNS using an anisotropic Maxwell model that can be interpreted as the extension of the viscous anisotropic model with an elastic component. The numerical simulation with this extended anisotropic model showed considerably less drag reduction than the original viscous model.

The mean velocity profile obtained with the viscoelastic model is not in accordance with experimental results: it shows a slight increase in mean velocity only in the region around $y^+ = 40$. The r.m.s. profiles of the viscoelastic model show the correct tendencies, although the changes caused by the viscoelastic model are smaller than those caused by the viscous anisotropic model. The same applies to the higher-order turbulence statistics and the stresses generated by the viscoelastic anisotropic model. However, the most important conclusion to be drawn from our viscoelastic simulation is that elasticity has an adverse effect on polymeric drag reduction when added to a viscous anisotropic fluid.

Indirect support for our main conclusion, stated in the first paragraph of this section, is the fact that other particles, such as fibres and surfactants, which also lead to drag reduction although less effectively than polymers, have in common with extended polymers that their shape is rod-like. This rod-like shape causes the relation between the deformation and the stresses in the flow to become anisotropic. In this respect, one may ask why fibres are not the best drag reducers, since these have, according to our conclusion, the required property. The answer in our opinion is that a polymer, stretched out by the flow, might be viewed as the ultimate fibre, since its aspect ratio can become much larger than that of a regular fibre. As a result polymers may be more effective than fibres in causing changes in the fluid stresses.

Our conclusion confirms the idea of Lumley (1969) that polymer stretching plays a key role in polymer drag reduction although not with the effect of increasing the viscosity as supposed by Lumley. The main result of our study supports, more specifically, the work of Landahl (1973), who arrived at a similar conclusion as ours after an investigation of the influence of different constitutive models on the stability of a conceptually simple turbulent flow model. Our results are also consistent with the findings of Sasaki (1991*a, b*, 1992), who arrived at essentially the same conclusions on the basis of gross-flow measurements of various polymer solutions. The ideas of de Gennes (1990), who attributes the effects of the polymers to an elastic modulus and not to a viscous mechanism, are not confirmed by our numerical experiments. However, we must note that our viscoelastic anisotropic model does not have an elastic modulus for shear, and hence is unable to support shear waves. The model only shows elastic effects in flow deformations with an extensional component. To investigate the effect of shear waves, a more complicated model is needed.

Some other evidence in support of our results is a recent computational study by Hinch (1994) who suggests that viscous effects may dominate elastic effects in extensional flows of dilute polymer solutions in general. This would indicate that our viscoelastic anisotropic model, even though it is simple, actually captures the most essential feature of a dilute polymer solution, at least in extensional flows.

Orlandi (1995) recently performed a direct numerical simulation in a so-called 'minimal channel', and obtained a drag reduction using a simple non-Newtonian fluid model. The constitutive equation used by Orlandi also contains anisotropic effects. Hence, Orlandi's results are compatible with our conclusions. However, Orlandi's model contains various mixed effects, and therefore he was not able to assess the influence of the anisotropy separately and draw the specific conclusions that we do.

A fact that remains unclear is how the existence of an onset Reynolds number can

be explained in terms of our viscous anisotropic model. It seems that such an onset criterion does not exist for our model, because the polymeric part of the equations will start to contribute to the physical process as soon as the flow becomes turbulent. This is consistent with the measurements by Virk & Wagger (1990) of dilute solutions of extended polymers. For randomly coiled polymers, however, an onset Reynolds number does indeed exist. This is another indication that the polymers must be extended for drag reduction. In that case the onset criterion determines when the polymers actually become extended by the flow. As proposed by Lumley (1973), and later confirmed by Berman & George (1974), this extension and hence the onset of drag reduction occurs when the ratio of turbulence and polymer time scales is of order one. This also means that polymers that already are extended by some other cause, for instance a chemical one, give drag reduction as soon as the flow becomes turbulent, as observed by Virk & Wagger (1990).

Finally, on the basis of our results and the preceding discussion, we propose the following mechanism for drag reduction by polymer additives. The polymers become extended by the flow at a certain Reynolds number, depending on the time scale of the polymer molecules in relation to the time scale of the turbulence. Hence, this 'onset' phenomenon is determined by the elastic properties of the fluid. When the polymers are extended, viscous anisotropic effects introduced by the extended polymers in the relation between the stress and the deformation cause a change in turbulence structure and the enstrophy production leading to a reduction in drag. At this stage, elasticity seems to play a counterproductive role in the drag reduction process.

At this stage our proposed mechanism of drag reduction can be only taken as a plausible but tentative explanation using the evidence that we have offered, but more information is needed. For instance, the mechanism of the onset of drag reduction as proposed here should be investigated. In addition more elaborate studies using more realistic constitutive models should be considered in future studies, when the advance in computer technology has relaxed computational restrictions. Possible candidates for such a studies are for example the full model proposed by Hinch (1994) or molecular polymer models.

The Academic Computing Services Centre (SARA) in Amsterdam and the National Computer Facilities (NCF) are gratefully acknowledged for the availability of the computer facilities and the financial support under grant SC-219 respectively. NCF is also thanked for assigning a special pilot project on the Cray Y-MP C98/4256, which has made it possible to initiate the present simulations. The research in this article was supported by the Foundation for Fundamental Research on Matter (FOM). Finally, we thank the following people for useful discussions and valuable support: Professor R. B. Bird, Professor B. H. A. A. van den Brule, Dr A. A. Draad and Dr J. G. M. Eggels.

REFERENCES

- BARK, F. H. & TINOCO, H. 1978 Stability of plane Poiseuille flow of a dilute suspension of slender fibres. *J. Fluid Mech.* **87**, 321–333.
- BATCHELOR, G. K. 1971 The stress generated in a non-dilute suspension of elongational particles by pure straining motion. *J. Fluid Mech.* **46**, 813–829.
- BERMAN, N. S. & GEORGE, JR., W. K. 1974 Onset of drag reduction in dilute polymer solutions. *Phys. Fluids* **17**, 250–251.

- DRAAD, A. A. 1996 Laminar-turbulent transition in pipe flow for Newtonian and non-Newtonian fluids. PhD thesis, Delft University of Technology.
- DRAAD, A. A. & HULSEN, M. A. 1995 Transition from laminar to turbulent flow for non-Newtonian fluids. In *Advances in Turbulence V* (ed. R. Benzi), pp. 105–110. Kluwer.
- DURST, F., JOVANOVIĆ, J. & SENDER, J. 1993 Detailed measurements of the near wall region of turbulent pipe flow. In *Data for Validation of CFD Codes* (ed. D. Goldstein, D. Hughes, R. Johnson & D. Lankford). ASME.
- EGGELS, J. G. M. 1994 Direct and large eddy simulation of turbulent flow in a cylindrical pipe geometry. PhD thesis, Delft University of Technology.
- EGGELS, J. G. M., UNGER, F., WEISS, M. H., WESTERWEEEL, J., ADRIAN, R. J., FRIEDRICH, R. & NIEUWSTADT, F. T. M. 1994 Fully developed turbulent pipe flow: a comparison between direct numerical simulation and experiment. *J. Fluid Mech.* **268**, 175–209.
- FRUMAN, D. H. & BARIGAH, M. 1982 Rheological interpretation of pressure anomalies of aqueous dilute polymer solutions (ADPS) in orifice flow. *Rheol. Acta* **21**, 556–560.
- GENNES, P. G. DE 1990 *Introduction to Polymer Dynamics*. Cambridge University Press.
- HARDER, K. J. & TIEDERMAN, W. G. 1991 Drag reduction and turbulent structure in two-dimensional channel flows. *Phil. Trans. R. Soc. Lond. A* **336**, 19–34.
- HINCH, E. J. 1977 Mechanical models of dilute polymer solutions in strong flows. *Phys. Fluids* **20**, S22–S30.
- HINCH, E. J. 1994 Uncoiling a polymer molecule in a strong extensional flow. *J. Non-Newtonian Fluid Mech.* **54**, 209–230.
- JAMES, D. F. & SARINGER, J. H. 1980 Extensional flow of dilute polymer solutions. *J. Fluid Mech.* **97**, 655–671.
- JOSEPH, D. D. 1990 *Fluid Dynamics of Viscoelastic Liquids*. Springer.
- JOSEPH, D. D., NARAIN, A., RICCIUS, O. & ARNEY, M. 1986 Shear-wave speeds and elastic moduli for different liquids. Theory and experiments. *J. Fluid Mech.* **171**, 289–338.
- KEILLER, R. A. & HINCH, E. J. 1991 Corner flow of a suspension of rigid rods. *J. Non-Newtonian Fluid Mech.* **40**, 323–335.
- KIM, J., MOIN, P. & MOSER, R. 1987 Turbulence statistics in fully developed channel flow at low Reynolds number. *J. Fluid Mech.* **177**, 133–166.
- LANDAHL, M. T. 1973 Drag reduction by polymer addition. In *Theoretical and Applied Mechanics, Proc. 13th Intl. Congr. Theor. and Appl. Mech.* (ed. E. Becker & G. K. Mikhailov), pp. 177–199. Springer.
- LIPSCOMB, G. G., DENN, M. M., HUR, D. U. & BOGER, D. V. 1988 The flow of fiber suspensions in complex geometries. *J. Non-Newtonian Fluid Mech.* **26**, 297–325.
- LUMLEY, J. L. 1969 Drag reduction by additives. *Ann. Rev. Fluid Mech.* **1**, 367–384.
- LUMLEY, J. L. 1972 On the solution of equations describing small scale deformation. In *Symposium Mathematica*, volume IX. Academic Press.
- LUMLEY, J. L. 1973 Drag reduction in turbulent flow by polymer additives. *Macromol. Rev.* **7**, 263–290.
- LUMLEY, J. L. & PANOFSKY, H. A. 1964 *The Structure of Atmospheric Turbulence*. Interscience Publishers.
- METZNER, A. B. & METZNER, A. P. 1970 Stress levels in rapid extensional flows of polymeric fluids. *Rheol. Acta* **9**, 174–181.
- ORLANDI, P. 1995 A tentative approach to the direct simulation of drag reduction by polymers. *J. Non-Newtonian Fluid Mech.* **60**, 277–301.
- PAPANASTASIOU, T. S. & ALEXANDROU, A. N. 1987 Isothermal extrusion of non-dilute fiber suspensions. *J. Non-Newtonian Fluid Mech.* **25**, 313–328.
- PERRY, A. E. & ABELL, C. J. 1975 Scaling laws for pipe flow turbulence. *J. Fluid Mech.* **67**, 257–271.
- PINHO, F. T. & WHITELAW, J. H. 1990 Flow of non-Newtonian fluids in a pipe. *J. Non-Newtonian Fluid Mech.* **34**, 129–144.
- POURQUIÉ, M. J. B. M. 1994 Large-eddy simulation of a turbulent jet. PhD thesis, Delft University of Technology.
- RUDD, M. J. 1972 Velocity measurements made with a laser Dopplermeter on the turbulent pipe flow of a dilute polymer solution. *J. Fluid Mech.* **51**, 673–685.
- SASAKI, S. 1991a Drag reduction effect of rod-like polymer solutions. I. Influences of polymer concentration and rigidity of skeletal back bone. *J. Phys. Soc. Japan* **60**, 868–878.

- SASAKI, S. 1991*b* Drag reduction effect of rod-like polymer solutions. II. Comparison between microgel and linear type polyions. *J. Phys. Soc. Japan* **60**, 2613–2618.
- SASAKI, S. 1992 Drag reduction effect of rod-like polymer solutions. III. Molecular weight dependence. *J. Phys. Soc. Japan* **61**, 1960–1963.
- SCHUMANN, U. 1975 Linear stability of finite difference equations for three-dimensional flow problems. *J. Comput. Phys.* **18**, 465–470.
- STOVER, C. A., KOCH, D. L. & COHEN, C. 1992 Observations of fibre orientation in simple shear flow of semi-dilute suspensions. *J. Fluid Mech.* **238**, 277–296.
- TENNEKES, H. & LUMLEY, J. L. 1972 *A First Course in Turbulence*. MIT Press.
- TIEDERMAN, W. G. 1990 The effect of dilute polymer solutions on viscous drag and turbulence structure. In *Structure of Turbulence and Drag Reduction* (ed. A. Gyr). IUTAM Symp., pp. 187–200. Springer.
- TOONDER, J. M. J. DEN 1995 Drag reduction by polymer additives in a turbulent pipe flow: laboratory and numerical experiments. PhD thesis, Delft University of Technology.
- TOONDER, J. M. J. DEN & NIEUWSTADT, F. T. M. 1996 Reynolds number effects in a turbulent pipe flow for low to moderate *Re*. *Phys. Fluids*. Submitted for publication.
- TOONDER, J. M. J. DEN, DRAAD, A. A., KUIKEN, G. D. C. & NIEUWSTADT, F. T. M. 1995*a* Degradation effects of dilute polymer solutions on turbulent drag reduction in pipe flows. *Appl. Sci. Res.* **55**, 63–82.
- TOONDER, J. M. J. DEN, NIEUWSTADT, F. T. M. & KUIKEN, G. D. C. 1995*b* The role of elongational viscosity in the mechanism of drag reduction by polymer additives. *Appl. Sci. Res.* **54**, 95–123.
- TOONDER, J. M. J. DEN, KUIKEN, G. D. C. & NIEUWSTADT, F. T. M. 1996 A criterion for identifying strong flow regions in turbulence. *Eur. J. Mech. B/Fluids* **15**, 735–753.
- VIRK, P. S. 1975 Drag reduction fundamentals. *AIChE J.* **21**, 625–656.
- VIRK, P. S. & WAGGER, D. L. 1990 Aspects of mechanisms in type B drag reduction. In *Structure of Turbulence and Drag Reduction* (ed. A. Gyr). IUTAM Symp., pp. 201–213. Springer.
- WEI, T. & WILLMARTH, W. W. 1992 Modifying turbulent structure with drag-reducing polymer additives in turbulent channel flows. *J. Fluid Mech.* **245**, 619–641.
- XU, C., TOONDER, J. M. J. DEN, NIEUWSTADT, F. T. M. & ZHANG, Z. 1996 Origin of high kurtosis levels in the viscous sublayer. Direct numerical simulation and experiment. *Phys. Fluids* **8**, 1938–1944.